Geophys. J. Int. (1999) **139,** 806–822

Introduction to the spectral element method for three-dimensional seismic wave propagation

Dimitri Komatitsch and Jeroen Tromp

Department of Earth and Planetary Sciences, Harvard University, Cambridge, MA 02138, *USA. E-mail: komatits@seismology.harvard.edu*

Accepted 1999 July 14. Received 1999 July 12; in original form 1999 March 29

SUMMARY

We present an introduction to the spectral element method, which provides an innovative numerical approach to the calculation of synthetic seismograms in 3-D earth models. The method combines the flexibility of a finite element method with the accuracy of a spectral method. One uses a weak formulation of the equations of motion, which are solved on a mesh of hexahedral elements that is adapted to the free surface and to the main internal discontinuities of the model. The wavefield on the elements is discretized using high-degree Lagrange interpolants, and integration over an element is accomplished based upon the Gauss–Lobatto–Legendre integration rule. This combination of discretization and integration results in a diagonal mass matrix, which greatly simplifies the algorithm. We illustrate the great potential of the method by comparing it to a discrete wavenumber/reflectivity method for layer-cake models. Both body and surface waves are accurately represented, and the method can handle point force as well as moment tensor sources. For a model with very steep surface topography we successfully benchmark the method against an approximate boundary technique. For a homogeneous medium with strong attenuation we obtain excellent agreement with the analytical solution for a point force.

Key words: attenuation, finite element methods, numerical techniques, seismic modelling, seismic wave propagation, topography.

1 INTRODUCTION

In both regional and global seismology, the accurate calculation of seismograms in realistic 3-D earth models has become a necessity. A large collection of numerical techniques is available for this purpose. Among them, the most widely used approach is probably the finite difference method (e.g. Kelly *et al.* 1976; Virieux 1986). This approach has been used to calculate the wavefield in 3-D local and regional models (e.g. Olsen & Archuleta 1996; Graves 1996; Ohminato & Chouet 1997). Unfortunately, significant difficulties arise in the presence of surface topography (Robertsson 1996) and when anisotropy needs to be incorporated (Igel *et al.* 1995). Pseudospectral methods have become popular for regional (Carcione 1994; Tessmer & Kosloff 1994) and global (Tessmer *et al.* 1992; Furumura *et al.* 1998) problems, but are restricted to models with smooth variations. Because of the problems associated with the implementation of the free-surface boundary condition, the accurate representation of surface waves in both finite difference (FD) and pseudospectral methods is a difficult problem and an active area of research (Robertsson 1996; Graves 1996; Komatitsch *et al.* 1996). Boundary integral methods provide an elegant approach for incorporating topographic variations, but are restricted to a finite number of homogeneous regions. In three dimensions, the numerical cost is high and approximations need to be made that lead to artefacts in the solution (Bouchon *et al.* 1996). Classical finite element methods have been successfully applied to the study of wave propagation in 3-D sedimentary basins (Bao *et al.* 1998). These techniques surmount some of the previously mentioned difficulties, but come with a high computational cost due to the fact that large linear systems need to be solved. The implementation of such algorithms on parallel computers with distributed memory complicates matters further (Bao *et al.* 1998). A promising new approach that combines aspects of FD, finite element and discrete wavenumber modelling has been proposed to reduce significantly the cost of the simulations (Moczo *et al.* 1997). Another approach is the direct solution method developed by Geller & Ohminato (1994) specifically for problems in global seismology. As usual in a Galerkin method, it involves the manipulation of large matrices and an approximate treatment of boundary undulations.

The spectral element method discussed in this article has been used for more than 15 years in computational fluid dynamics (Patera 1984). It has recently gained interest for problems related to 2-D (Seriani *et al.* 1992; Cohen *et al.* 1993; Priolo *et al.* 1994) and 3-D (Komatitsch 1997; Faccioli *et al.* 1997; Komatitsch & Vilotte 1998; Seriani 1998; Komatitsch

et al. 1999c; Paolucci *et al.* 1999) seismic wave propagation. The method easily incorporates free-surface topography and accurately represents the propagation of surface waves. The effects of anisotropy (Seriani *et al.* 1995; Komatitsch *et al.* 1999b) and fluid–solid boundaries (Komatitsch *et al.* 1999a) can also be accommodated. The method lends itself well to parallel computation with distributed memory (Fischer & Rønquist 1994; Seriani 1997; Komatitsch & Vilotte 1998).

The purpose of this article is to give a detailed introduction to the spectral element method in the context of seismic wave propagation. We demonstrate the accuracy of the method for both body and surface waves by comparing its results against those of a discrete wavenumber/reflectivity method (Bouchon 1981; Müller 1985) for simple layer-cake models. Simulations for a full moment tensor source are compared against results based upon a frequency–wavenumber and an FD method (Graves 1996) for a dip-slip source in a half-space. We also demonstrate that the method can handle steep topography by analysing the effects of a hemispherical crater embedded in a half-space on an incident plane compressional wave, and comparing the results to those obtained with an approximate boundary method (Sánchez-Sesma 1983). Finally, we show that strong attenuation can be taken into account by simulating a 2-D homogeneous medium with $Q_P \simeq 30$ and $Q_S \simeq 20$ and comparing the results to the analytical solution for a point source force derived by Carcione *et al.* (1988).

2 EQUATIONS OF MOTION

We seek to determine the displacement field produced by an earthquake in a finite earth model with volume Ω, as shown in Fig. 1. The boundaries of this volume include a stress-free surface $\partial\Omega$, as well as an absorbing boundary Γ. Seismic waves are reflected by the free surface $\partial\Omega$; ideally, they are completely absorbed by the artificial boundary Γ. The unit outward normal to the boundary $\partial\Omega+\Gamma$ is denoted by $\hat{\mathbf{n}}$. The earth model may have any number of internal discontinuities; the unit upward normal to such discontinuities is also denoted by $\hat{\mathbf{n}}$. Locations within the model are denoted by the position vector $\mathbf{x}=(x, y, z)$. For brevity, a component of the position vector will sometimes be denoted using index notation: x_i, $i=1, 2, 3$, where $x_1=x$, $x_2=y$, and $x_3=z$. Unit vectors in the directions of increasing x_i are denoted by $\hat{\mathbf{x}}_i$, and partial derivatives with respect to x_i are denoted by ∂_i.

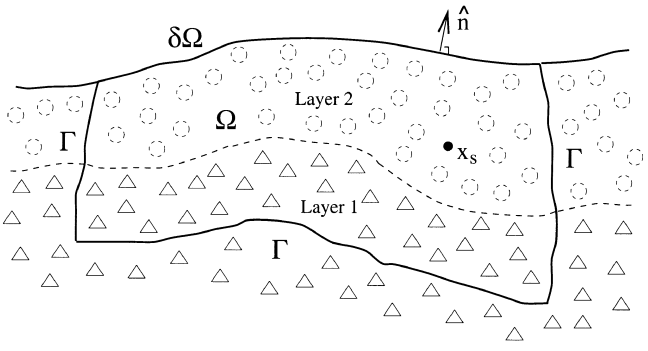

Figure 1. Finite earth model with volume Ω and free surface $\partial\Omega$. An artificial absorbing boundary Γ is introduced, and $\hat{\mathbf{n}}$ denotes the unit outward normal to all boundaries. The model can be fully heterogeneous or composed of any number of layers. The source $\mathbf{x}_\mathbf{s}$ can be placed anywhere inside Ω.

The equations of motion that govern the propagation of seismic waves in an elastic or anelastic solid may be solved based upon either a *strong* or a *weak* formulation of the problem. In the strong formulation one works directly with the equations of motion and associated boundary conditions written in differential form; this approach is used, for instance, in FD or global pseudospectral modelling techniques. In the weak formulation one uses an integral form of the equations of motion, as in finite element (FEM) and direct solution methods. The spectral element method (SEM) discussed in this article is based upon a weak formulation of the equations of motion. We shall ignore the effects of fluid regions and associated fluid–solid boundaries, although the SEM can be used to solve such problems (Komatitsch *et al.* 1999a).

2.1 Strong form

The displacement field $\mathbf{s}$ produced by an earthquake is governed by the momentum equation,

$$\rho\,\partial_t^2\mathbf{s}=\boldsymbol{\nabla}\cdot\mathbf{T}+\mathbf{f}\,. \tag{1}$$

The distribution of density is denoted by ρ. The stress tensor $\mathbf{T}$ is linearly related to the displacement gradient $\boldsymbol{\nabla}\mathbf{s}$ by Hooke's law, which in an elastic, anisotropic solid may be written in the form

$$\mathbf{T}=\mathbf{c}:\boldsymbol{\nabla}\mathbf{s}\,. \tag{2}$$

The elastic properties of the earth model are determined by the fourth-order elastic tensor $\mathbf{c}$, which has 21 independent components in the case of general anisotropy. Modelling wave propagation in fully anisotropic media with classical techniques such as the FD method is difficult because of the use of staggered grids (Igel *et al.* 1995). The SEM, on the other hand, can accurately model the effects of any anisotropy on elastic waves (Komatitsch *et al.* 1999b).

In an attenuating medium, Hooke's law (2) needs to be modified such that the stress is determined by the entire strain history:

$$\mathbf{T}(t)=\int_{-\infty}^{t}\partial_t\mathbf{c}(t-t'):\boldsymbol{\nabla}\mathbf{s}(t')\,dt'\,. \tag{3}$$

In seismology, the quality factor Q is observed to be constant over a wide range of frequencies. Such an *absorption-band solid* may be mimicked by a series of L standard linear solids (Liu *et al.* 1976). In practice, two or three linear solids usually suffice to obtain an almost constant Q (Emmerich & Korn 1987). The components of the anelastic tensor for such a series may be written in the form

$$c_{ijkl}(t)=c^{\mathrm{R}}_{ijkl}\left[1-\sum_{\ell=1}^{L}\left(1-\tau^{\epsilon\ell}_{ijkl}/\tau^{\sigma\ell}\right)\mathrm{e}^{-t/\tau^{\sigma\ell}}\right]H(t)\,, \tag{4}$$

where c^{R}_{ijkl} denotes the relaxed modulus and $H(t)$ is the Heaviside function. The stress relaxation times $\tau^{\sigma\ell}$ are chosen to be the same for all components of the anelastic tensor, whereas the strain relaxation times $\tau^{\epsilon\ell}_{ijkl}$ are unique to each individual component. In practice, attenuation in the earth is mainly controlled by the shear quality factor, such that only the time dependence of the isotropic shear modulus need be accommodated.

A factor 1/L is not included before the sum in eqs (4) and (7) here, as in most of pre-2005 literature (see e.g. Moczo and Kristek, GRL, vol. 32, p. L01306 (2005) for an explanation). However it has been shown by Chang-Hua Zhang et al. (SEG meeting abstract, 2016) that both options (including it or not) are fine and lead to the same final result at the end.

Using the absorption-band anelastic tensor (4), the constitutive relation (3) may be rewritten in the form

$$\mathbf{T} = \mathbf{c}^{\mathrm{U}} : \boldsymbol{\nabla}\mathbf{s} - \sum_{\ell=1}^{L} \mathbf{R}^{\ell}, \tag{5}$$

where for each standard linear solid

$$\partial_t \mathbf{R}^{\ell} = -\mathbf{R}^{\ell}/\tau^{\sigma\ell} + \boldsymbol{\delta}\mathbf{c}^{\ell} : \boldsymbol{\nabla}\mathbf{s}/\tau^{\sigma\ell}. \tag{6}$$

The components of the unrelaxed modulus c^{U}_{ijkl} are given by

$$c^{\mathrm{U}}_{ijkl} = c^{\mathrm{R}}_{ijkl}\left[1 - \sum_{\ell=1}^{L} (1 - \tau^{\epsilon\ell}_{ijkl}/\tau^{\sigma\ell})\right], \tag{7}$$

and the modulus defect $\boldsymbol{\delta}\mathbf{c}^{\ell}$ associated with each individual standard linear solid is determined by

$$\delta c^{\ell}_{ijkl} = -c^{\mathrm{R}}_{ijkl}(1 - \tau^{\epsilon\ell}_{ijkl}/\tau^{\sigma\ell}). \tag{8}$$

The earthquake source is represented by the point force $\mathbf{f}$, which may be written in terms of a moment tensor $\mathbf{M}$ as

$$\mathbf{f} = -\mathbf{M} \cdot \boldsymbol{\nabla}\delta(\mathbf{x} - \mathbf{x}_{\mathrm{s}}) S(t). \tag{9}$$

The location of the point source is denoted by $\mathbf{x}_{\mathrm{s}}$, $\delta(\mathbf{x} - \mathbf{x}_{\mathrm{s}})$ denotes the Dirac delta distribution located at $\mathbf{x}_{\mathrm{s}}$, and the source time function is given by $S(t)$. A finite source may be simulated by using a number of point sources, each with its own time history.

The momentum equation (1) must be solved subject to a stress-free boundary condition at the earth's surface $\partial\Omega$:

$$\mathbf{T} \cdot \hat{\mathbf{n}} = \mathbf{0}. \tag{10}$$

In FD and global pseudospectral applications, the implementation of the free-surface condition (10), especially in the presence of surface topography, is a difficult problem and an active area of research (e.g. Carcione 1994; Tessmer & Kosloff 1994; Komatitsch *et al.* 1996; Moczo *et al.* 1997; Ohminato & Chouet 1997).

At every internal boundary, both the displacement $\mathbf{s}$ and the traction $\mathbf{T} \cdot \hat{\mathbf{n}}$ need to be continuous. At the artificial model boundary Γ, waves travelling out of the volume Ω need to be absorbed. The implementation of an efficient absorbing boundary is not an easy problem (Clayton & Engquist 1977; Quarteroni *et al.* 1998; Komatitsch *et al.* 1999c). The approximate absorbing boundary condition we shall use relates traction to velocity,

$$\mathbf{T} \cdot \hat{\mathbf{n}} = \rho[v_n(\hat{\mathbf{n}} \cdot \partial_t \mathbf{s})\hat{\mathbf{n}} + v_1(\hat{\mathbf{t}}_1 \cdot \partial_t \mathbf{s})\hat{\mathbf{t}}_1 + v_2(\hat{\mathbf{t}}_2 \cdot \partial_t \mathbf{s})\hat{\mathbf{t}}_2], \tag{11}$$

where $\hat{\mathbf{t}}_1$ and $\hat{\mathbf{t}}_2$ are orthogonal unit vectors tangential to the absorbing boundary Γ with unit outward normal $\hat{\mathbf{n}}$, v_n is the quasi-P wave speed of waves travelling in the $\hat{\mathbf{n}}$ direction, v_1 is the quasi-S wave speed of waves polarized in the $\hat{\mathbf{t}}_1$ direction, and v_2 is the quasi-S wave speed of waves polarized in the $\hat{\mathbf{t}}_2$ direction. The absorbing boundary condition (11) is based upon a one-way treatment that perfectly absorbs waves impinging at right angles to the boundary, but that is less effective for waves that graze the boundary (Clayton & Engquist 1977). It is valid for transversely isotropic media with a horizontal or vertical symmetry axis; more general anisotropy can be accommodated by tapering it such that the medium becomes transversely isotropic on the absorbing boundary Γ. Note that one can use attenuation close to the artificial absorbing boundary of the model to increase the efficiency of the approximate absorbing condition (11).

2.2 Weak form

Rather than using the equations of motion and associated boundary conditions directly, one can use an integrated form. This is accomplished by dotting the momentum equation (1) with an arbitrary test vector $\mathbf{w}$, integrating by parts over the model volume Ω, and imposing the stress-free boundary condition (10) and the absorbing boundary condition expressed in terms of traction (11). This gives

$$\begin{aligned}\int_{\Omega} \rho\, \mathbf{w} \cdot \partial_t^2 \mathbf{s}\, d^3\mathbf{x} &= -\int_{\Omega} \boldsymbol{\nabla}\mathbf{w} : \mathbf{T}\, d^3\mathbf{x} + \mathbf{M} : \boldsymbol{\nabla}\mathbf{w}(\mathbf{x}_{\mathrm{s}})\, S(t) \\ &\quad + \int_{\Gamma} \rho[v_n(\hat{\mathbf{n}} \cdot \partial_t \mathbf{s})\hat{\mathbf{n}} + v_1(\hat{\mathbf{t}}_1 \cdot \partial_t \mathbf{s})\hat{\mathbf{t}}_1 + v_2(\hat{\mathbf{t}}_2 \cdot \partial_t \mathbf{s})\hat{\mathbf{t}}_2] \cdot \mathbf{w}\, d^2\mathbf{x},\end{aligned} \tag{12}$$

where the stress tensor $\mathbf{T}$ is determined in terms of the displacement gradient $\boldsymbol{\nabla}\mathbf{s}$ by Hooke's law (2). The source term, $\int_{\Omega} \mathbf{f} \cdot \mathbf{w}\, d^3\mathbf{x}$, has been explicitly integrated using the properties of the Dirac delta distribution. Slip on a finite fault plane may be simulated by making the substitution

$$\mathbf{M} : \boldsymbol{\nabla}\mathbf{w}(\mathbf{x}_{\mathrm{s}})\, S(t) \rightarrow \int_{S_{\mathrm{s}}} \mathbf{m}(\mathbf{x}_{\mathrm{s}}, t) : \boldsymbol{\nabla}\mathbf{w}(\mathbf{x}_{\mathrm{s}})\, d^2\mathbf{x}_{\mathrm{s}}, \tag{13}$$

where S_{s} denotes the fault surface and $\mathbf{m}(\mathbf{x}_{\mathrm{s}}, t)$ denotes the moment density tensor.

Mathematically, the strong and the weak formulations are equivalent because (12) holds for *any* test vector $\mathbf{w}$. However, one of the nice features of the weak formulation is that the stress-free surface boundary condition (10) is naturally satisfied; that is, it does not have to be imposed explicitly. The incorporation of free-surface topography is therefore straightforward, and surface waves are more accurately simulated than in methods based upon the strong form (Komatitsch & Vilotte 1998; Komatitsch *et al.* 1999c).

The weak form of the equations of motion (12) remains valid in an anelastic earth model, except that the stress tensor $\mathbf{T}$ is in this case determined by the absorption-band constitutive relation (5), and that memory in the system is accounted for by eq. (6). This approach has been used in the context of finite element simulations by Moczo *et al.* (1997) and Kay & Krebes (1999), and is more satisfactory than the use of a simple damping matrix (Bao *et al.* 1998; Faccioli *et al.* 1997), which results in a Q that strongly depends on frequency. The main drawback of the approach, however, is the additional computer memory requirement resulting from the use of several memory variables per gridpoint. Spreading the memory variables over neighbouring gridpoints has been suggested to reduce this requirement (Zeng 1996; Day 1998).

3 DEFINITION OF THE MESH

As in a classical FEM, the model volume Ω is subdivided into a number of non-overlapping elements Ω_e, $e = 1, \ldots, n_e$, such that $\Omega = \bigcup_e^{n_e} \Omega_e$, as shown in Fig. 2. As a result of this subdivision, the absorbing boundary Γ is similarly represented by a number of surface elements Γ_b, $b = 1, \ldots, n_b$, such that $\Gamma = \bigcup_b^{n_b} \Gamma_b$. In a FEM, a variety of elements such as tetrahedra

A factor 1/L is not included before the sum in eqs (4) and (7) here, as in most of pre-2005 literature (see e.g. Moczo and Kristek, GRL, vol. 32, p. L01306 (2005) for an explanation). However it has been shown by Chang-Hua Zhang et al. (SEG meeting abstract, 2016) that both options (including it or not) are fine and lead to the same final result at the end.

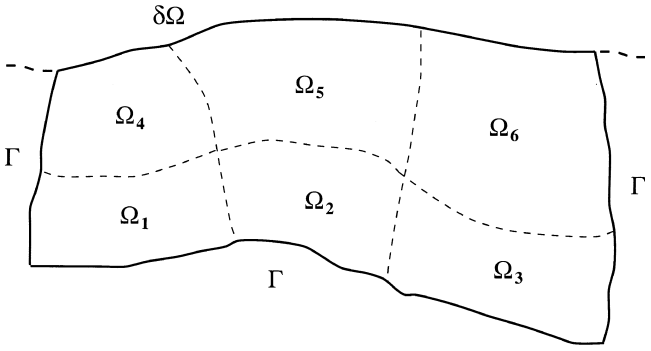

Figure 2. For the purpose of computations, the earth model Ω shown in Fig. 1 is subdivided into curved elements (quadrangles in 2-D, hexahedra in 3-D) whose shapes are adapted to the edges of the model $\partial\Omega$ and Γ, as well as to the main geological interfaces.

or hexahedra can be used (e.g. Dhatt & Touzot 1984), but a SEM is restricted to hexahedral volume elements Ω_e. Consequently, the absorbing boundary Γ is subdivided in terms of quadrilateral surface elements Γ_b.

In the next two sections we briefly describe how boundary and volume elements are parametrized. In what follows the reader should keep in mind that by 'boundary elements' we simply mean the sides of some of the volume elements. The results in this section may be found in any finite element text book (Zienkiewicz 1977; Hughes 1987). We include them here in an effort to provide a more complete overview of the SEM.

3.1 Boundary elements

Each quadrilateral boundary element is isomorphous to the square, hence there exists a unique mapping from the square to each surface element Γ_b, $b=1, \ldots, n_b$. The reference square is defined in terms of greek coordinates (ξ, η), $-1\le\xi\le1$, $-1\le\eta\le1$, which are sometimes referred to as the *natural coordinates*. Each quadrilateral element Γ_b is defined in terms of a set of n_a *control points* or *anchors* $\mathbf{x}_a=\mathbf{x}(\xi_a, \eta_a)$, $a=1, \ldots, n_a$, and a set of n_a *shape functions* $N_a(\xi, \eta)$. Its four corners are always used as anchors, but its side centres and its centre may be used as additional anchors. For simple boundary elements with straight edges, four control points suffice, whereas for curved boundary elements nine control points may be needed to describe their shape accurately. Fig. 3 illustrates quadrilateral elements defined in terms of four and nine control points. For any given boundary element, the relation between a point $\mathbf{x}$ within the element Γ_b and a point (ξ, η) in the reference square Λ may therefore be written in the form

$$\mathbf{x}(\xi, \eta)=\sum_{a=1}^{n_a} N_a(\xi, \eta)\mathbf{x}_a\,. \tag{14}$$

The shape functions $N_a(\xi, \eta)$ are products of Lagrange polynomials of degrees 1 or 2. The $n_\ell+1$ Lagrange polynomials of degree n_ℓ are defined in terms of $n_\ell+1$ control points $-1\le\xi_\alpha\le1$, $\alpha=0, \ldots, n_\ell$, by

$$\ell_\alpha^{n_\ell}(\xi)=\frac{(\xi-\xi_0)\cdots(\xi-\xi_{\alpha-1})(\xi-\xi_{\alpha+1})\cdots(\xi-\xi_{n_\ell})}{(\xi_\alpha-\xi_0)\cdots(\xi_\alpha-\xi_{\alpha-1})(\xi_\alpha-\xi_{\alpha+1})\cdots(\xi_\alpha-\xi_{n_\ell})}\,. \tag{15}$$

Notice from this definition that when the Lagrange polynomials are evaluated at a control point ξ_β they return a value of either 0 or 1:

$$\ell_\alpha^{n_\ell}(\xi_\beta)=\delta_{\alpha\beta}\,, \tag{16}$$

where δ denotes the Kronecker delta. The two Lagrange polynomials of degree 1 with two control points, $\xi=-1$ and $\xi=1$, are $\ell_0^1(\xi)=(1-\xi)/2$ and $\ell_1^1(\xi)=(1+\xi)/2$, and the three Lagrange polynomials of degree 2 with three control points, $\xi=-1$, $\xi=0$ and $\xi=1$, are $\ell_0^2(\xi)=\xi(\xi-1)/2$, $\ell_1^2(\xi)=1-\xi^2$ and $\ell_2^2(\xi)=\xi(\xi+1)/2$. As an example, the four shape functions associated with the four-anchor quadrilateral element shown in Fig. 3 are products of degree 1 Lagrange polynomials: $N_1(\xi, \eta)=\ell_0^1(\xi)\ell_0^1(\eta)$, $N_2(\xi, \eta)=\ell_1^1(\xi)\ell_0^1(\eta)$, $N_3(\xi, \eta)=\ell_1^1(\xi)\ell_1^1(\eta)$ and $N_4(\xi, \eta)=\ell_0^1(\xi)\ell_1^1(\eta)$. Similarly, the shape functions of nine-anchor quadrilateral elements are products of degree 2 Lagrange polynomials.

The orientation of the reference square Λ is chosen such that the unit outward normal $\hat{\mathbf{n}}$ to boundary element Γ_b is given by

$$\hat{\mathbf{n}}=\frac{1}{J_b}\frac{\partial\mathbf{x}}{\partial\xi}\times\frac{\partial\mathbf{x}}{\partial\eta}\,, \tag{17}$$

where J_b denotes the Jacobian of the transformation

$$J_b=\left\|\frac{\partial\mathbf{x}}{\partial\xi}\times\frac{\partial\mathbf{x}}{\partial\eta}\right\|. \tag{18}$$

The boundary elements should be defined in such a way that the Jacobian J_b never vanishes. As in a classical FEM, this places important constraints on the mesh generation process (Hughes 1987), which are further discussed later. To calculate the Jacobian J_b and the unit outward normal $\hat{\mathbf{n}}$ one needs to determine the six partial derivatives $\partial\mathbf{x}/\partial\xi$ and $\partial\mathbf{x}/\partial\eta$. This is accomplished by differentiating the mapping (14):

$$\begin{aligned}\partial_\xi\mathbf{x}(\xi, \eta)&=\sum_{a=1}^{n_a}\partial_\xi N_a(\xi, \eta)\mathbf{x}_a\,,\\ \partial_\eta\mathbf{x}(\xi, \eta)&=\sum_{a=1}^{n_a}\partial_\eta N_a(\xi, \eta)\mathbf{x}_a\,.\end{aligned} \tag{19}$$

Partial derivatives of the shape functions, $\partial_\xi N_a$ and $\partial_\eta N_a$, are analytically determined in terms of Lagrange polynomials of degrees 1 or 2 and their derivatives.

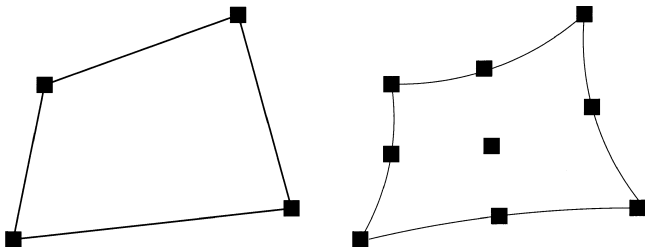

Figure 3. The geometry of each of the curved surface quadrangles can be defined by either four control nodes (left) or nine control nodes (right).

3.2 Volume elements

Similarly, each hexahedral volume element Ω_e can be mapped to a reference cube. Points within this reference cube are denoted by the vector $\boldsymbol{\xi}=(\xi, \eta, \zeta)$, where $-1\le\xi\le1$, $-1\le\eta\le1$ and $-1\le\zeta\le1$. The components of the vector $\boldsymbol{\xi}$ will sometimes be denoted using index notation: ξ_i, $i=1, 2, 3$, where $\xi_1=\xi$,

$\xi_2=\eta$, $\xi_3=\zeta$. Analogous to the boundary elements discussed in the previous section, each volume element is defined in terms of n_a anchors $\mathbf{x}_a=\mathbf{x}(\xi_a, \eta_a, \zeta_a)$, $a=1, \ldots, n_a$, and shape functions $N_a(\boldsymbol{\xi})$. At least eight corner nodes are needed to define a hexahedral volume element; by adding mid-side and centre nodes the number of anchors can become as large as 27. Fig. 4 illustrates eight-node and 27-node hexahedral elements. The mapping between points within the hexahedral element and the reference cube may be written in the form

$$\mathbf{x}(\boldsymbol{\xi})=\sum_{a=1}^{n_a} N_a(\boldsymbol{\xi})\mathbf{x}_a\,. \tag{20}$$

Shape functions of eight-node hexahedral elements are triple products of degree 1 Lagrange polynomials, and those of 27-node hexahedral elements are triple products of degree 2 Lagrange polynomials. Frequently one uses a reduced 20-node element (Dhatt & Touzot 1984), which is obtained by eliminating seven centre nodes from the 27-node element, as illustrated in Fig. 4.

An element of volume $dx\,dy\,dz$ within a given element Ω_e is related to an element of volume $d\xi\,d\eta\,d\zeta$ in the reference cube by

$$dx\,dy\,dz=J_e\,d\xi\,d\eta\,d\zeta\,, \tag{21}$$

where the volumetric Jacobian J_e is given by

$$J_e=\left|\frac{\partial(x, y, z)}{\partial(\xi, \eta, \zeta)}\right|. \tag{22}$$

To calculate the Jacobian J_e, we need the partial derivative matrix $\partial\mathbf{x}/\partial\boldsymbol{\xi}$, which is obtained by differentiating the mapping (20):

$$\frac{\partial\mathbf{x}}{\partial\boldsymbol{\xi}}=\sum_{a=1}^{n_a}\frac{\partial N_a}{\partial\boldsymbol{\xi}}\,\mathbf{x}_a\,. \tag{23}$$

Partial derivatives of the shape functions are determined analytically in terms of Lagrange polynomials of degree 1 or 2 and their derivatives. The elements should be constructed in such a way that the Jacobian J_e never vanishes, which again poses strong constraints on the mesh generation process. This ensures that the mapping from the reference cube to the element, $\mathbf{x}(\boldsymbol{\xi})$, is unique and invertible, that is, $\boldsymbol{\xi}(\mathbf{x})$ is well defined.

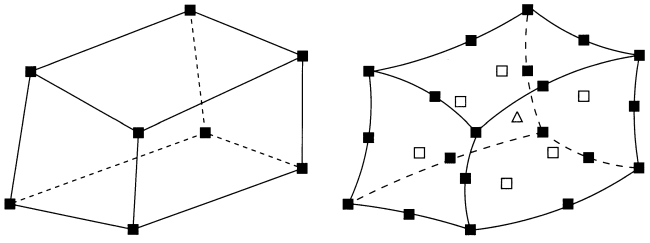

Figure 4. The geometry of each of the curved volume hexahedra can be defined by either eight control nodes (left) or 27 control nodes (right). In the case of the 27-node brick, the empty squares indicate the six nodes that lie in the middle of the sides of the element, and the triangle indicates the node that lies at the centre of the element. By ignoring these nodes, one obtains the classical 20-node element that can also be used to define the geometry.

4 REPRESENTATION OF FUNCTIONS ON THE ELEMENTS

To solve the weak form of the equations of motion (12), integrations over the volume Ω and the absorbing boundary Γ are subdivided in terms of smaller integrals over the volume and surface elements Ω_e and Γ_b, respectively. This section is concerned with the representation of functions on the elements, and with the integration of functions over an element.

We have seen in the previous section that the shape of the boundary and volume elements can be defined in terms of low-degree Lagrange polynomials. In a traditional FEM, low-degree polynomials are also used as basis functions for the representation of fields on the elements. In a SEM, on the other hand, a higher-degree Lagrange interpolant is used to express functions on the elements. Of course, one could use the same high-degree polynomial representation to define the geometrical mapping on each element, but in practice such high precision is unnecessary, provided the variations in element geometry are smooth enough.

For reasons discussed in Sections 5 and 6, the control points ξ_α, $\alpha=0, \ldots, n_\ell$, needed in the definition (15) of the Lagrange polynomials of degree n_ℓ are chosen to be the $n_\ell+1$ Gauss–Lobatto–Legendre points, which are the roots of

$$(1-\xi^2)P'_{n_\ell}(\xi)=0\,, \tag{24}$$

where P'_{n_ℓ} denotes the derivative of the Legendre polynomial of degree n_ℓ. These points can be computed by numerical resolution of (24) (Canuto *et al.* 1988, p. 61). Note that the Gauss–Lobatto–Legendre points always include $+1$ and -1; therefore in a SEM some points always lie exactly on the boundaries of the elements. As an example, Fig. 5 illustrates the nine Lagrange polynomials of degree 8 based upon the nine Gauss–Lobatto–Legendre control points defined by (24).

4.1 Polynomial representation on elements

On boundary elements Γ_b, a function f is interpolated by products of Lagrange polynomials of degree n_ℓ as

$$f(\mathbf{x}(\xi, \eta))\approx\sum_{\alpha,\beta=0}^{n_\ell} f^{\alpha\beta}\ell_\alpha(\xi)\ell_\beta(\eta)\,. \tag{25}$$

For convenience, the polynomial degree n_ℓ has been omitted as a superscript on the Lagrange polynomials. As a result of the definition (16) of the Lagrange polynomials, the coefficients $f^{\alpha\beta}$ are the functional values of f at the interpolation points $\mathbf{x}(\xi_\alpha, \eta_\beta)$:

$$f^{\alpha\beta}=f(\mathbf{x}(\xi_\alpha, \eta_\beta))\,. \tag{26}$$

In a SEM for wave propagation problems one typically uses a polynomial degree n_ℓ between 5 and 10 to represent a function on the element (Seriani & Priolo 1994; Komatitsch & Vilotte 1998). Similarly, on each volume element Ω_e a function f is interpolated by triple products of Lagrange polynomials of degree n_ℓ as

$$f(\mathbf{x}(\xi, \eta, \zeta))\approx\sum_{\alpha,\beta,\gamma=0}^{n_\ell} f^{\alpha\beta\gamma}\ell_\alpha(\xi)\ell_\beta(\eta)\ell_\gamma(\zeta),$$

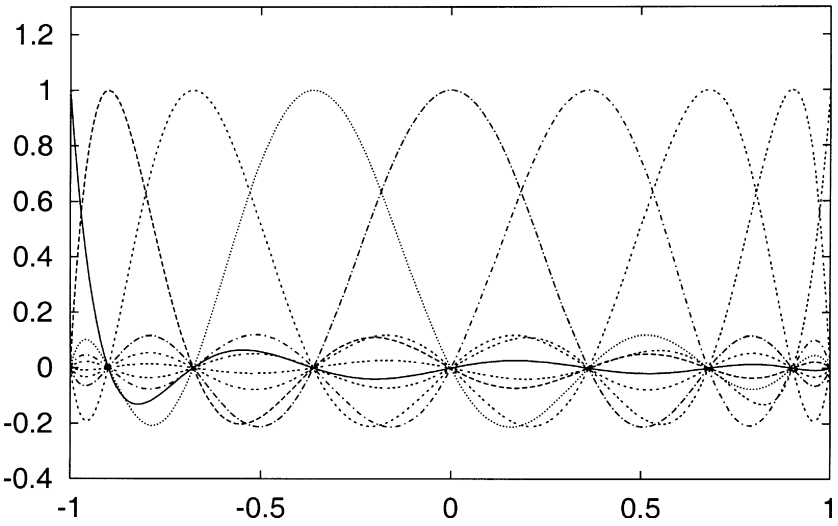

Figure 5. Lagrange interpolants of degree $N=8$ at the Gauss–Lobatto–Legendre points on the reference segment $[-1, 1]$. The $N+1=9$ Gauss–Lobatto–Legendre points can be distinguished along the horizontal axis. All Lagrange polynomials are, by definition, equal to 1 or 0 at each of these points.

where

$$f^{\alpha\beta\gamma} = f(\mathbf{x}(\xi_\alpha, \eta_\beta, \zeta_\gamma)) \,. \tag{27}$$

Using this polynomial representation, the gradient of a function, ∇f, may be written in the form

$$\begin{aligned} \nabla f(\mathbf{x}(\xi, \eta, \zeta)) &\approx \sum_{i=1}^{3} \hat{\mathbf{x}}_i \partial_i f(\mathbf{x}(\xi, \eta, \zeta)) \\ &= \sum_{i=1}^{3} \hat{\mathbf{x}}_i \sum_{\alpha,\beta,\gamma=0}^{n_\ell} f^{\alpha\beta\gamma} [\ell'_\alpha(\xi)\ell_\beta(\eta)\ell_\gamma(\zeta)\partial_i\xi \\ &\quad + \ell_\alpha(\xi)\ell'_\beta(\eta)\ell_\gamma(\zeta)\partial_i\eta + \ell_\alpha(\xi)\ell_\beta(\eta)\ell'_\gamma(\zeta)\partial_i\zeta] \,, \end{aligned} \tag{28}$$

where a prime denotes differentiation. When evaluated at any of the Gauss–Lobatto–Legendre points $\mathbf{x}(\xi_{\alpha'}, \eta_{\beta'}, \zeta_{\gamma'})$, this expression reduces to

$$\begin{aligned} \nabla f(\mathbf{x}(\xi, \eta, \zeta)) \approx \sum_{i=1}^{3} \hat{\mathbf{x}}_i \Bigg[&\sum_{\alpha=0}^{n_\ell} f^{\alpha\beta'\gamma'} \ell'_\alpha(\xi_{\alpha'})\partial_i\xi + \sum_{\beta=0}^{n_\ell} f^{\alpha'\beta\gamma'} \ell'_\beta(\eta_{\beta'})\partial_i\eta \\ &+ \sum_{\gamma=0}^{n_\ell} f^{\alpha'\beta'\gamma} \ell'_\gamma(\zeta_{\gamma'})\partial_i\zeta \Bigg] \,. \end{aligned} \tag{29}$$

Notice that in (29), which is based upon the chain rule, one needs the inverse Jacobian matrix $\partial\boldsymbol{\xi}/\partial\mathbf{x}$. This matrix is obtained by inverting the Jacobian matrix $\partial\mathbf{x}/\partial\boldsymbol{\xi}$, which is determined in terms of the shape functions by (23). This inverse exists provided the Jacobian J_e is non-singular, which is a requirement for the proper design of the mesh, as mentioned previously.

4.2 Integration over elements

At this stage, integrations over surface elements Γ_b may be approximated using the Gauss–Lobatto–Legendre integration rule,

$$\begin{aligned} \int_{\Gamma_b} f(\mathbf{x})\, d^2\mathbf{x} &= \int_{-1}^{1}\int_{-1}^{1} f(\mathbf{x}(\xi, \eta))\, J_b(\xi, \eta)\, d\xi\, d\eta \\ &\approx \sum_{\alpha,\beta=0}^{n_\ell} \omega_\alpha\omega_\beta f^{\alpha\beta} J_b^{\alpha\beta} \,, \end{aligned} \tag{30}$$

where ω_α, $\alpha=0, \ldots, n_\ell$, denote the weights associated with the Gauss–Lobatto–Legendre points of integration, and $J_b^{\alpha\beta} = J_b(\xi_\alpha, \eta_\beta)$. These weights are computed numerically (Canuto *et al.* 1988, p. 61).

Similarly, integrations over volume elements Ω_e may be approximated as

$$\begin{aligned} \int_{\Omega_e} f(\mathbf{x})\, d^3\mathbf{x} &= \int_{-1}^{1}\int_{-1}^{1}\int_{-1}^{1} f(\mathbf{x}(\xi, \eta, \zeta))\, J_e(\xi, \eta, \zeta)\, d\xi\, d\eta\, d\zeta \\ &\approx \sum_{\alpha,\beta,\gamma=0}^{n_\ell} \omega_\alpha\omega_\beta\omega_\gamma f^{\alpha\beta\gamma} J_e^{\alpha\beta\gamma} \,, \end{aligned} \tag{31}$$

where $J_e^{\alpha\beta\gamma} = J_e(\xi_\alpha, \eta_\beta, \zeta_\gamma)$. To facilitate the integration of functions and their partial derivatives over the elements, the values of the inverse Jacobian matrix $\partial\boldsymbol{\xi}/\partial\mathbf{x}$ need to be determined at the $(n_\ell+1)^3$ Gauss–Lobatto–Legendre integration points for each element.

5 GLOBAL SYSTEM AND TIME MARCHING

We have seen that in a SEM the model is subdivided in terms of a number of hexahedral elements. On each individual element, functions are sampled at the Gauss–Lobatto–Legendre points of integration. Gridpoints that lie on the sides, edges or corners of an element are shared amongst neighbouring elements, as illustrated in Fig. 6. Therefore, the need arises to distinguish between the gridpoints that define an element, the *local mesh*, and all the gridpoints in the model, many of which are shared

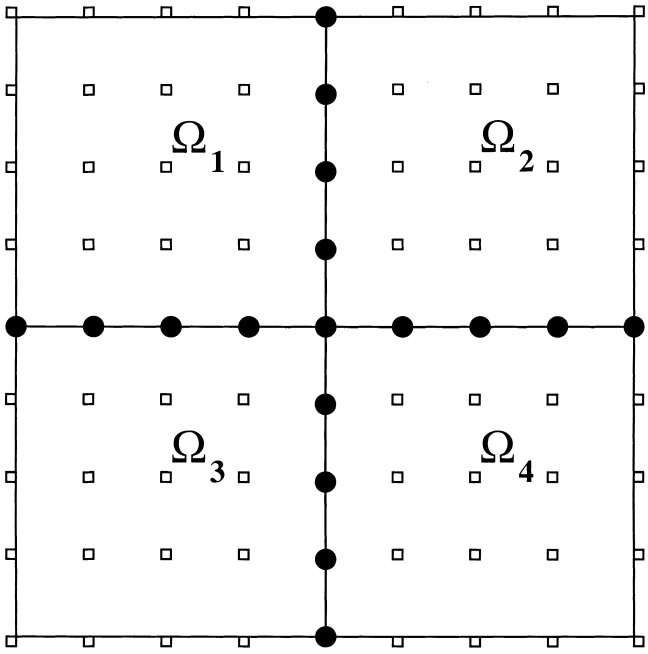

Figure 6. Illustration of the local and global meshes for a four-element 2-D spectral element discretization with polynomial degree $N=4$. Each spectral element contains $(N+1)^2=25$ Gauss–Lobatto–Legendre points, which constitute the local mesh for each element. These points are non-evenly spaced, but have been drawn evenly spaced here for simplicity. In the global mesh, points lying on edges or corners (as well as on faces in three dimensions) are shared between elements. The contributions to the global system of degrees of freedom, computed separately on each element, have to be summed at these common points represented by black dots. Exactly two elements share points inside an edge in two dimensions, while corners can be shared by any number of elements depending on the topology of the mesh, which can be non-structured.

amongst several spectral elements, the *global mesh*. One needs to determine a mapping between gridpoints in the local mesh and gridpoints in the global mesh; efficient routines are available for this purpose from finite element modelling. Before the system can be marched forward in time, the contributions from all the elements that share a common global gridpoint need to be summed. In a traditional FEM this is referred to as the *assembly* of the system. Computationally, this assembly stage is a costly part of the calculation on parallel computers because information from individual elements needs to be shared with neighbouring elements, an operation that involves communication between distinct CPUs.

Let U denote the displacement vector of the global system; that is, U contains the displacement vector at all the gridpoints in the global mesh, classically referred to as the *global degrees of freedom* of the system. The ordinary differential equation that governs the time dependence of the global system may be written in the form

$$M\ddot{U}+C\dot{U}+KU=F, \tag{32}$$

where M denotes the global mass matrix, C the global absorbing boundary matrix, K the global stiffness matrix and F the source term. Explicit expressions for the local contributions to the stiffness matrix, the source and the absorbing boundaries are given in the Appendix. Further details on the construction of the global mass and stiffness matrices from their elemental forms may be found in Komatitsch & Vilotte (1998).

A highly desirable property of a SEM, which allows for a very significant reduction in the complexity and cost of the algorithm, is the fact that the mass matrix M is diagonal by construction. Therefore, no costly linear system resolution algorithm is needed to march the system in time. At the elemental level, the mass matrix is given by the first term in the weak formulation of the equations of motion (12):

$$\int_{\Omega_e} \rho\,\mathbf{w}\cdot\partial_t^2\mathbf{s}\,d^3\mathbf{x} = \int_{-1}^{1}\int_{-1}^{1}\int_{-1}^{1} \rho(\mathbf{x}(\boldsymbol{\xi}))\,\mathbf{w}(\mathbf{x}(\boldsymbol{\xi}))\cdot\partial_t^2\mathbf{s}(\mathbf{x}(\boldsymbol{\xi}),\,t)\,J(\boldsymbol{\xi})\,d^3\boldsymbol{\xi}\,. \tag{33}$$

The displacement $\mathbf{s}$ is expanded on an element as

$$\mathbf{s}(\mathbf{x}(\xi,\,\eta,\,\zeta),\,t)\approx\sum_{j=1}^{3}\hat{\mathbf{x}}_j\sum_{\sigma,\tau,\nu=0}^{n_\ell}s_j^{\sigma\tau\nu}(t)\ell_\sigma(\xi)\ell_\tau(\eta)\ell_\nu(\zeta)\,. \tag{34}$$

Similarly, we choose test functions of the form

$$\mathbf{w}(\mathbf{x}(\xi,\,\eta,\,\zeta))=\sum_{i=1}^{3}\hat{\mathbf{x}}_i\sum_{\alpha,\beta,\gamma=0}^{n_\ell}w_i^{\alpha\beta\gamma}\ell_\alpha(\xi)\ell_\beta(\eta)\ell_\gamma(\zeta)\,. \tag{35}$$

Upon substituting (35) and (34) into (33), and introducing the Gauss–Lobatto–Legendre numerical integration, we find that

$$\begin{aligned}
&\int_{\Omega_e}\rho\,\mathbf{w}\cdot\partial_t^2\mathbf{s}\,d^3\mathbf{x}\\
&\approx\sum_{\alpha',\beta',\gamma'}\omega_{\alpha'}\omega_{\beta'}\omega_{\gamma'}J_e^{\alpha'\beta'\gamma'}\rho^{\alpha'\beta'\gamma'}\sum_{i,j=1}^{3}\hat{\mathbf{x}}_i\cdot\hat{\mathbf{x}}_j\\
&\quad\times\sum_{\alpha,\beta,\gamma}w_i^{\alpha\beta\gamma}\ell_\alpha(\xi_{\alpha'})\ell_\beta(\eta_{\beta'})\ell_\gamma(\zeta_{\gamma'})\sum_{\sigma,\tau,\nu}\ddot{s}_j^{\sigma\tau\nu}(t)\ell_\sigma(\xi_{\alpha'})\ell_\tau(\eta_{\beta'})\ell_\nu(\zeta_{\gamma'})\\
&=\sum_{\alpha',\beta',\gamma'}\omega_{\alpha'}\omega_{\beta'}\omega_{\gamma'}J_e^{\alpha'\beta'\gamma'}\rho^{\alpha'\beta'\gamma'}\sum_{i,j=1}^{3}\delta_{ij}\sum_{\alpha,\beta,\gamma}w_i^{\alpha\beta\gamma}\delta_{\alpha\alpha'}\delta_{\beta\beta'}\delta_{\gamma\gamma'}\\
&\quad\times\sum_{\sigma,\tau,\nu}\ddot{s}_i^{\sigma\tau\nu}(t)\delta_{\sigma\alpha'}\delta_{\tau\beta'}\delta_{\nu\gamma'}\\
&=\sum_{\alpha,\beta,\gamma}\omega_\alpha\omega_\beta\omega_\gamma J_e^{\alpha\beta\gamma}\rho^{\alpha\beta\gamma}\sum_{i=1}^{3}w_i^{\alpha\beta\gamma}\ddot{s}_i^{\alpha\beta\gamma}(t)\,,
\end{aligned} \tag{36}$$

where $\rho^{\alpha\beta\gamma}=\rho(\mathbf{x}(\xi_\alpha,\,\eta_\beta,\,\zeta_\gamma))$, and where a dot denotes differentiation with respect to time. It is important to realize that the weak form of the equations of motion holds for *any* test vector $\mathbf{w}$. Therefore, the global system (32) is built by independently setting factors of $w_1^{\alpha\beta\gamma}$, $w_2^{\alpha\beta\gamma}$ and $w_3^{\alpha\beta\gamma}$ equal to zero. What is remarkable about the result (36) is the fact that the value of acceleration at each point, $\ddot{s}_i^{\alpha\beta\gamma}(t)$, is simply multiplied by the factor $\omega_\alpha\omega_\beta\omega_\gamma\rho^{\alpha\beta\gamma}J_e^{\alpha\beta\gamma}$; that is, the elemental mass matrix is diagonal. This property also holds true for the global mass matrix after assembly of the system. It is this desirable property that has motivated the use of Lagrange interpolants for the representation of functions on the elements, in conjunction with the use of the Gauss–Lobatto–Legendre integration rule. Note that density ρ need not be constant over an element, but may vary from one gridpoint to another. Therefore, the SEM is able to handle fully heterogeneous media.

In this study, time discretization of the second-order ordinary differential equation (32) is achieved based upon a classical explicit second-order FD scheme, moving the stiffness and absorbing terms to the right-hand side. Such a scheme is conditionally stable, and the Courant stability condition is governed by the minimum value of the ratio between the size of the grid cells and the *P*-wave velocity. In some cases, for instance when very small cells are needed in high wave-speed regions, the Courant stability condition may be too restrictive for an explicit scheme. In that case a Newmark scheme, written in prediction–multicorrection format, can be used instead (Komatitsch 1997; Komatitsch *et al.* 1999a). For anelastic media, we separately march the strong form of the memory variable eq. (6) in time, regarding the term in $\mathbf{\nabla s}$ as a source, as proposed by Robertsson *et al.* (1994). These first-order equations in time are integrated based upon a fourth-order Runge–Kutta scheme that is known to be efficient for this problem (Carcione 1994).

6 ACCURACY OF THE METHOD

6.1 Selection of the polynomial degree

In a SEM, spatial resolution is controlled by two parameters: the typical size of an element, Δh, and the polynomial degree used to represent functions on an element, n_ℓ, each element thus containing $n_\ell + 1$ points in each direction. In this respect, SEMs are related to FEMs based upon a high polynomial degree, the so-called *h-p* version of FEM (Guo & Babuška 1986). In practice, if the polynomial degree n_ℓ is too small, e.g. less than typically 4, a SEM exhibits the same inaccuracies that are observed in a standard FEM applied to wave propagation problems (Marfurt 1984). On the other hand, if the polynomial degree is very large, e.g. greater than 15, the method is spatially very accurate, but the computational requirements become prohibitive. The reason for this is that the evaluation of the stiffness matrix at the elemental level has a cost of $O(n_\ell^4)$ in three dimensions due to the matrix multiplications involved. Typically, polynomial degrees between 5 and 10 are therefore optimal for a SEM applied to wave propagation problems, because this provides the best trade-off between accuracy and cost (Seriani & Priolo 1994). In order to obtain accurate results, Δh has to be chosen such that the average number of points per minimum wavelength $\lambda_{\min}$ in an element, $\lambda_{\min} = (n_\ell + 1)/\Delta h$, is roughly equal to 5 for the optimal range of polynomial degrees mentioned above (Seriani & Priolo 1994; Faccioli *et al.* 1997). Therefore, a SEM compares favourably with a high-order FD method in terms of the required number of points per wavelength.

6.2 Mesh design

In a SEM, as in any method based upon a mesh of elements, the design of the mesh is a critical and difficult step. The use of hexahedral elements required in a SEM—no tetrahedra are allowed—complicates matters further. Some expertise in mesh design or pre-processing of the model is required to ensure that the resolution provided by the mesh, in particular the number of gridpoints per wavelength, will be sufficient for the problem. For example, densification of the mesh is usually needed near the free surface, in areas of slow wave speed or strong contrasts in wave speed, in regions of steep topography, or near faults. In practice, one generally designs the mesh such that it honours the free surface and the main geological boundaries within the model. As in a traditional FEM, the curvature of the elements should be modest, such that the Jacobian of the mapping to the reference domain varies smoothly across any given element and never vanishes (Hughes 1987).

Because seismic wave speed generally increases with depth, one often needs to coarsen the grid in the deeper parts of the model to retain a similar number of gridpoints per wavelength. A simple way of accomplishing this in two stages consists of doubling the grid first in one horizontal dimension and, subsequently, at a greater depth, in the second horizontal dimension, as illustrated in Fig. 7. This mesh design will prove useful for studying a layer-cake model with low wave speeds near the surface in Section 7.1. However, this simple conforming mesh is not optimal because it contains 45° angles, and therefore high local variations in the size and shape of the spectral elements. In this respect, an area of active research involves the use of non-conforming meshes in which two or more elements share the same edge with another, larger element, or the combination of spectral element algorithms with other techniques such as classical FEMs (Bernardi *et al.* 1990; Lahaye et al. 1997; Chaljub & Vilotte 1998). These approaches simplify the coarsening of a mesh considerably, but are significantly more difficult to implement.

6.3 Accuracy of the integration

We have seen in Section 5 that the use of Lagrange interpolants for the representation of functions on an element, in conjunction with the use of a Gauss–Lobatto–Legendre numerical integration, results in a diagonal mass matrix, which in turn leads to a simple time integration scheme. This has been accomplished based upon the Gauss–Lobatto–Legendre integration rule, rather than the more classical Gauss rule that

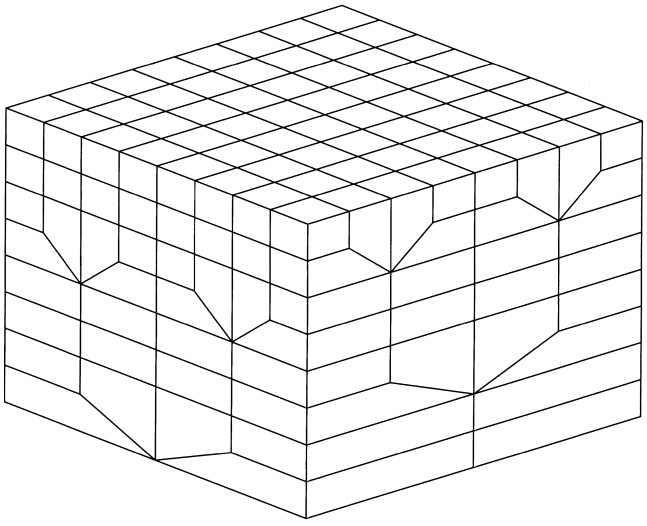

Figure 7. Non-structured brick used to define a mesh with smaller elements at the top of the structure, where velocities are usually smaller, and with bigger elements at the bottom, where velocities are usually larger. We apply a geometrical grid doubling first in one of the horizontal directions and then in the other. Here this coarsening in depth has been applied twice; therefore, the elements at the bottom are four times bigger in the horizontal direction than the surface elements.

is used in a FEM. However, even on a square with homogeneous elastic properties, the Gauss–Lobatto–Legendre rule is exact only for polynomials of degree $2n_\ell - 1$. Each integration on the reference element involves the product of two polynomials of degree n_ℓ: the displacement and the test function. The integration of the resulting polynomial of degree $2n_\ell$ is never exact, even in this simple case. For deformed elements there are additional errors related to curvature (Maday & Rønquist 1990); the same is true for elements with heterogeneous material properties. Thus, a diagonal mass matrix has been obtained by a process of subintegration. In this respect, the SEM is related to FEMs in which mass lumping is used to avoid the costly resolution of the non-diagonal system resulting from the use of Gauss quadrature (Cohen *et al.* 1993).

It is interesting to note that even though a SEM exhibits high spatial accuracy, the time marching scheme we use to solve the resulting ordinary differential equation in time (32) is a simple second-order FD scheme. Therefore, in the long run the overall accuracy of the simulation is often mainly governed by the time scheme, and in this respect the use of more accurate, higher-order schemes, as suggested for instance by Tarnow & Simo (1994), could be of interest.

7 NUMERICAL RESULTS

In order to validate the method, we consider five numerical tests. In the first two tests, we study the response of two 1-D layer-cake models for both a shallow and a deep source. Solutions based upon a combined discrete wavenumber/reflectivity method are used for comparison. In the third test we study a dip-slip source in a homogeneous half-space in order to check the accuracy of the moment tensor source representation. Results based upon frequency–wavenumber and FD techniques are available for comparison. In the fourth test, we consider a hemispherical crater embedded in a homogeneous half-space in order to demonstrate the accuracy of the free-surface boundary condition in the presence of very steep topography. Results based upon an approximate boundary method are used as a reference. These first four tests are for purely elastic media. In the fifth and final test, we study strong attenuation in a 2-D homogeneous medium and compare the results to the analytical solution of the problem.

7.1 Layer-cake models

To demonstrate that the non-structured mesh described in Section 6.2 and represented in Fig. 7 is efficient for typical layered geological structures, we first study a simple model consisting of a layer over a half-space, as shown in Fig. 8 (left). The horizontal size of the block used is 134 km × 134 km, and the block extends to a depth of 60 km. Absorbing conditions are used on all sides of the model except the free surface. The non-structured mesh, whose coarsening in depth is implemented as shown in Fig. 7, is composed of 68 208 elements, using a polynomial degree $N = 5$, which results in a global grid composed of 8 743 801 points. In the first simulation, the source is a vertical force located in the half-space, in the middle of the grid at a depth of 25.05 km. Therefore, the solution will include strong multiples in addition to the direct P and S waves. The time variation of the source is a Ricker wavelet, that is, the second derivative of a Gaussian, with a dominant frequency $f_0 = 0.4$ Hz, and therefore a maximum frequency of the order of 1 Hz. The onset time of the source is $t_0 = 2.6$ s. The time step used is $\Delta t = 6.5$ ms, and we propagate the signal for 6150 time steps (i.e. 40 s). A line of receivers is placed at the surface along the y-axis at $x = x_{\max}/2 = 67$ km. The receivers record the three components of displacement.

Traces recorded at two receivers along the receiver line are shown in Fig. 9 for two of the components of the displacement vector, the third (tangential) component being zero by symmetry. The first receiver is located at a horizontal distance of 2.39 km from the source, the second at 31.11 km. The strong direct P and S waves can be clearly observed, as well as strong multiples generated by the layer. To check the accuracy of the simulation, we compare the SEM results to those based upon a discrete wavenumber method (Bouchon 1981) used in conjunction with a reflectivity method (Müller 1985). The agreement between the two results is very good, both for the direct waves and for the numerous multiples. Small parasitic phases reflected from the approximate absorbing conditions in our simulation probably explain the small discrepancies observed in the later arrivals between $t = 30$ and $t = 35$ s.

For the same model, we now place the source inside the layer, close to the surface, at a depth of 536.1 m. Thus the response includes a very significant surface wave contribution,

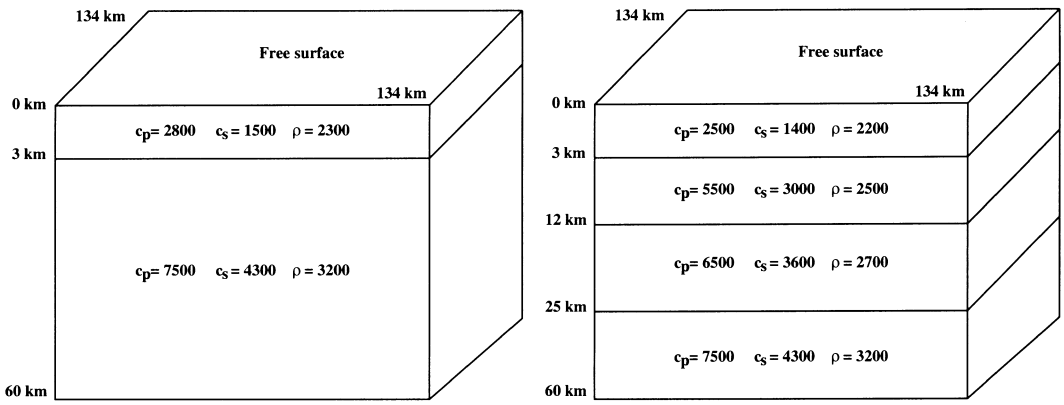

Figure 8. 3-D models with 1-D velocity structure used to assess the efficiency of the non-structured brick of Fig. 7. We study a model consisting of a layer over a half-space (left) as well as a three-layer model over a half-space (right). In both cases the horizontal size of the block is 134 km × 134 km, and it extends to a depth of 60 km.

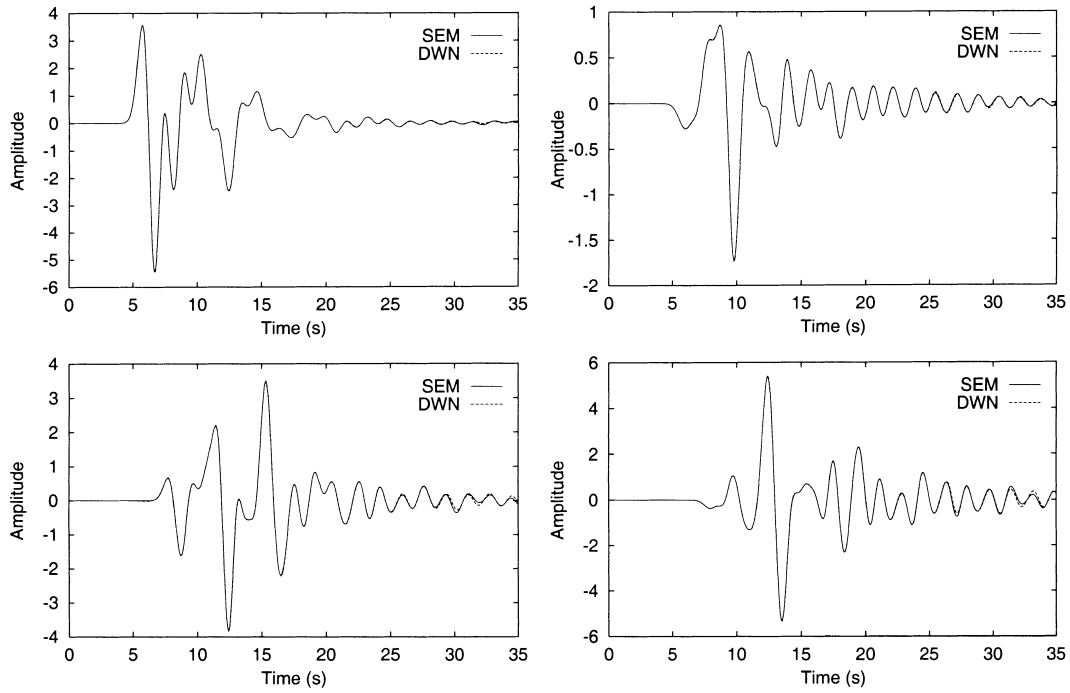

Figure 9. Traces recorded at the surface along the y-axis at $x = 67$ km for the model composed of a layer over a half-space (Fig. 8, left). The source is a vertical force located in the middle of the block at a depth of 25.05 km. The two receivers are located at horizontal distances of 2.39 km (top) and 31.11 km (bottom) from the source. The vertical (left) and radial (right) components of displacement are compared to the solution computed using a discrete wavenumber method used in conjunction with the reflectivity method. The third (tangential) component is zero by symmetry. The direct P wave can be mainly observed on the vertical component, while the direct S wave has significant amplitude on both. Numerous strong multiples are clearly visible.

whose accuracy will again be checked against the discrete wavenumber/reflectivity method. Apart from the depth of the source, all parameters remain the same as in the first simulation. Traces recorded at the surface at two receivers located, respectively, at horizontal distances of 2.39 and 23.93 km from the source are shown in Fig. 10. The main phase is a strong surface wave, whose amplitude is much larger than that of the direct P and S waves. Significant surface wave dispersion can be observed due to the presence of the low-velocity layer over the faster half-space. The SEM solution is again in very good agreement with the discrete wavenumber/reflectivity reference.

In a second simulation, we study the more complex model consisting of three layers over a half-space illustrated in Fig. 8 (right). The non-structured mesh, which is based on the brick represented in Fig. 7, honours the three interfaces of the model at depths of 3, 12 and 25 km respectively. The grid doubling is applied twice in the layer situated between 3 and 12 km. Apart from the number of layers and their properties, all other parameters remain the same as before. We first study the displacement recorded at the surface in the case of vertically incident plane P or S waves coming from the bottom of the model. This test is interesting because, since the velocity model is 1-D and the incidence is vertical, no mode conversions occur, and therefore the solution is a superposition of pure P or pure S waves, which allows us to validate them separately. Furthermore, for normal incidence the absorbing condition (11) used at the bottom of the grid is exact, therefore in this test we have no spurious reflections off the boundaries. On the vertical edges of the grid we use periodic boundary conditions. We compute a very precise reference solution using a 1-D FD code with several hundred points per minimum wavelength. Fig. 11 shows the comparison at the surface for an incident plane P wave and for an incident plane S wave. Numerous multiples can be observed after the first arrival. The agreement with the FD solution is excellent. The amplification at the surface is very significant: the maximum displacement recorded is roughly 3.8 in both cases, for an incident value of 1.

We use the same three-layer model with a vertical force in the middle of the block at a depth of 20.16 km. Traces recorded at two receivers, located, respectively, at horizontal distances of 2.39 and 31.11 km from the source, are shown in Fig. 12, as well as a comparison with results obtained based upon the discrete wavenumber/reflectivity method. The agreement is again very good, even for this difficult structure, except for some small artefacts reflected off the absorbing boundaries in the SEM results between $t = 30$ and $t = 35$ s.

The above tests demonstrate that a SEM is capable of accurately simulating wave propagation in 3-D models at a reasonable cost. We implemented the parallel algorithm based upon OpenMP directives on shared memory architectures and the Message-Passing Interface (MPI) on distributed memory architectures. The total CPU time of each of these simulations using the MPI implementation on an eight-node Dec Alpha was roughly 8 hr. We obtained a total sustained performance of 1.3 Gigaflops, a parallel speedup of 7.3, and a parallel efficiency of 91 per cent. The total memory needed was roughly 1 Gbytes. The MPI code was also successfully run on a network of PCs under Linux (a so-called Beowulf machine).

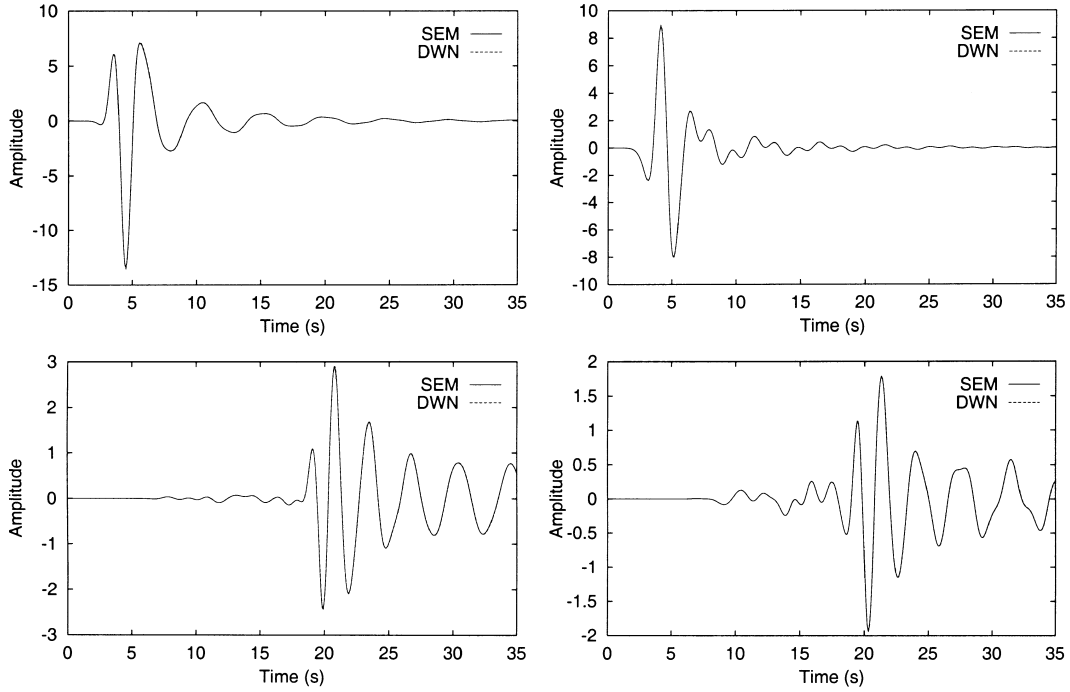

Figure 10. Traces recorded at the surface along the y-axis at $x=67$ km for the model composed of a layer over a half-space (Fig. 8, left). The source is a vertical force located in the sedimentary layer in the middle of the block at a depth of 536.1 m. The two receivers are located at horizontal distances of 2.39 km (top) and 23.93 km (bottom) from the source. The main event is a strong dispersive surface wave whose amplitude is several times bigger than that of the direct P and S waves. The vertical (left) and radial (right) components of displacement are compared to the solution computed using a discrete wavenumber method used in conjunction with the reflectivity method. The third (tangential) component is zero by symmetry.

7.2 Moment tensor source

As discussed in the Appendix, a moment tensor source can be naturally introduced in a SEM. To check the accuracy of the approach, we use a homogeneous half-space with P-wave velocity $c_p=4000$ m s^{-1}, S-wave velocity $c_s=2300$ m s^{-1} and density $\rho=1800$ kg m^{-3}. The source is placed at a depth of 2.5 km, and receivers are placed exactly at the surface, at a horizontal distance of 10 km. We use a pure dip-slip source (strike 90°, dip 90°, rake 90°) with scalar moment $M_0=10^{16}$ N m, and record the vertical and radial components of velocity at an azimuth of 0° and the tangential component at an azimuth of 90°. This problem has been studied previously by Graves (1996) using both an FD technique and a frequency–wavenumber (FK) technique; his results are used as a reference. The SEM mesh is a structured block of $42\times42\times22$ elements, with a polynomial degree $N=5$ used in each element. Therefore, the global grid is composed of 4 941 831 gridpoints. The mesh represents a block of size 42 km × 42 km × 22 km. The time step used is $\Delta t=5$ ms, and we propagate the signal for 2400 time steps (i.e. 12 s). The time dependence of the velocity source is a triangle with base width $t_b=1$ s and onset time $t_0=0.55$ s. Results are low-pass filtered at a cut-off frequency of $f_0=1$ Hz using a Butterworth filter, as in Graves (1996). In Fig. 13, we show the components of velocity obtained based upon the three techniques, without any normalization of the amplitude. The overall agreement is good, which validates the implementation of the moment tensor source in the SEM.

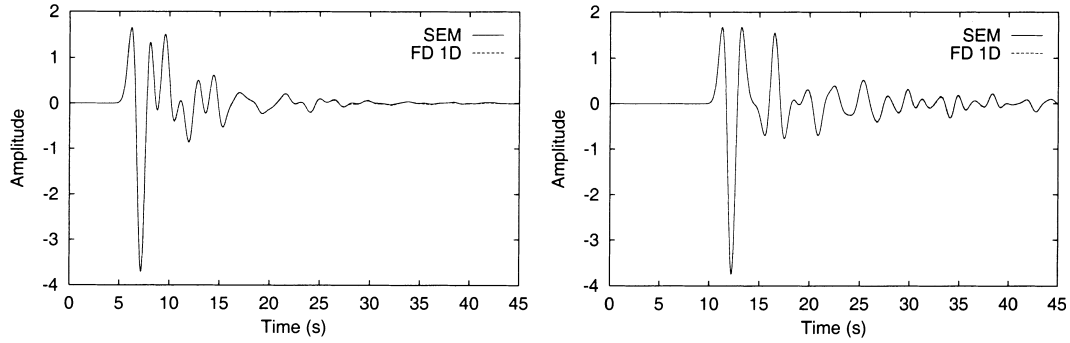

Figure 11. Response recorded at the surface of the model composed of three layers over a half-space (Fig. 8, right) due to plane P (left) and S (right) waves incident perpendicularly from below. A highly accurate 1-D FD solution is shown for comparison. The absorbing bottom boundary condition is exact in this case; periodic boundary conditions are applied at the four sides of the block. The incident plane wave has an amplitude of 1 and is amplified by a factor of roughly 3.8 near the surface.

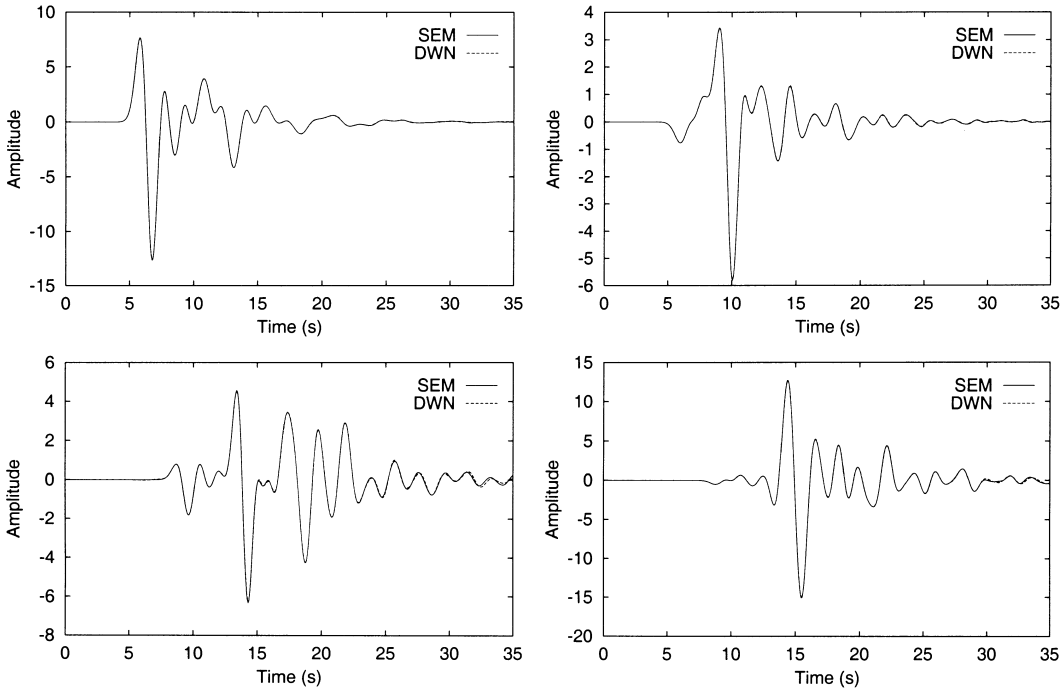

Figure 12. Traces recorded at the surface along the y-axis at $x=67$ km for the model composed of three layers over a half-space (Fig. 8, right). The source is a vertical force located in the middle of the block at a depth of 20.16 km. The two receivers are located at horizontal distances of 2.39 km (top) and 31.11 km (bottom) from the source. The vertical (left) and radial (right) components of displacement are compared to the solution computed using a discrete wavenumber method in conjunction with the reflectivity method. The third (tangential) component is zero by symmetry.

Some non-causal oscillations are present in the FK reference, in particular on the tangential component, which may explain the small discrepancies observed in the amplitude. These oscillations could perhaps be reduced by using a discrete wavenumber method to compute the reference. The FD results are slightly less accurate, mainly for the radial component, and show some parasitic later arrivals around $t=8$ s that are probably due to spurious reflections off the absorbing boundaries.

7.3 Hemispherical crater

Sánchez-Sesma (1983) studied the response of a hemispherical crater in a homogeneous half-space to a vertically incident plane P wave based upon an approximate boundary method. He presented the amplitude of the displacement recorded at the surface of the crater for different normalized frequencies $\eta=2a/\lambda_P$, where a denotes the radius of the crater and λ_P the wavelength of the incident P wave. His results have been used as a reference in several subsequent studies (Mossessian & Dravinski 1989; Luzón *et al.* 1997).

Mesh generation based upon conforming hexahedra is non-trivial for a sphere or a hemisphere. Fortunately, an elegant analytical mesh called the 'cubed sphere' has recently been developed (Ronchi *et al.* 1996). Such a mesh was first used by Chaljub & Vilotte (1998) for global wave propagation problems. We use the five sides of half a cubed sphere to mesh the hemisphere, as shown in Fig. 14. The global mesh is therefore composed of five structured blocks. A desirable property of such a mesh is that it takes into account the vertical edges of the crater at the free surface and is naturally refined in the vicinity of the crater, where a high degree of accuracy is needed to describe the geometry and to resolve amplification and mode conversions correctly. We compute the amplitude of the displacement at the surface along a profile for two values of the normalized frequency, $\eta=0.25$ and $\eta=0.50$, as a function of the normalized horizontal coordinate x/a between 0 and 2, starting at the centre of the crater. Poisson's ratio is equal to 0.25. The wavelengths considered are of the order of the radius of the crater. Therefore, the main concern in this simulation is not the resolution of the computations, that is, number of points per wavelength, but the correct description of the geometry of the hemisphere. In particular, this has a significant influence on the correct modelling of the surface waves generated by the incident P wave, travelling back and forth along the crater. We can therefore use very big elements in the half-space, but need to use small enough curved elements close to the crater to describe its shape correctly. To avoid artefacts related to artificial boundaries, considering a crater with a radius of $a=1$ km, we extend the model to a horizontal size of 32 km $\times$ 32 km, and a depth of 16 km. The mesh is composed of 1800 elements, with a polynomial degree $N=4$ in each element; the global mesh contains 120 089 gridpoints. Such a small value is again due to the fact that we have used a small number of big elements in this simulation. Periodic conditions are used on the four vertical sides of the global grid. Considering a P-wave velocity of $c_p=1732$ m s^{-1} and an S-wave velocity of $c_s=1000$ m s^{-1}, the time step used is $\Delta t=5$ ms, and the signal is propagated for 3200 time steps (i.e. 16 s). The density is 1000 kg m^{-3}. The source is an incident plane P wave, which is a Ricker wavelet in time with dominant frequency $f_0=\sqrt{3}/4$ Hz. It is introduced in the SEM as initial displacement and velocity fields in the time scheme. Seismograms are then converted to the frequency domain for comparison with Sánchez-Sesma (1983).

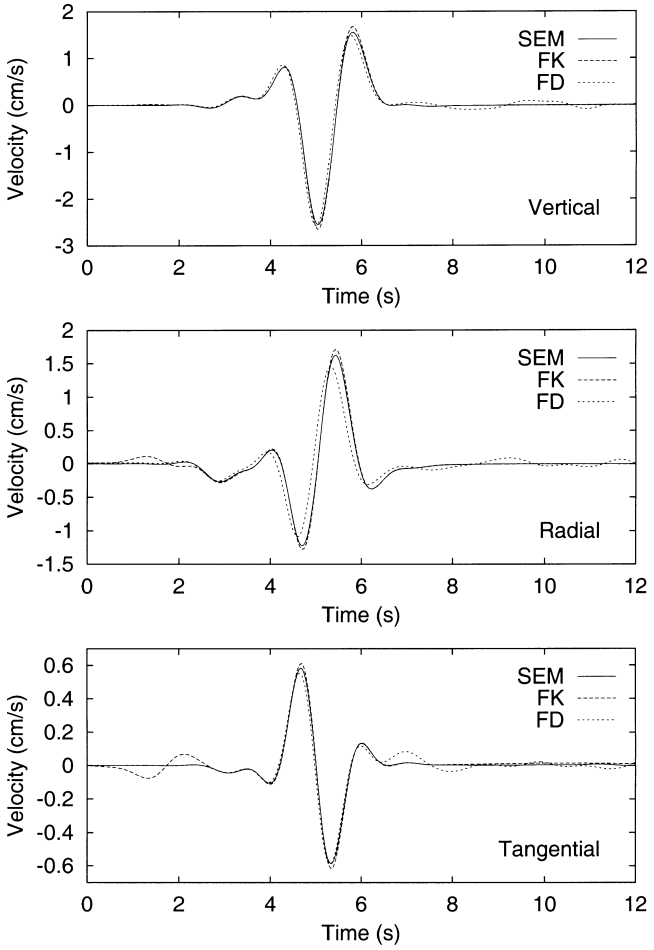

Figure 13. Spectral element (solid line), FK (dashed line) and FD (dotted line) results obtained at the surface of a homogeneous half-space in the case of a pure dip-slip moment tensor source situated at a depth of 2.5 km. The receivers are located at a horizontal distance of 10 km. The vertical (top) and radial (middle) components of velocity are recorded at an azimuth of 0°, while the tangential component (bottom) is recorded at an azimuth of 90°. The source is a triangular velocity pulse in time, and the results are low-pass filtered at a cut-off frequency of 1 Hz. The FK and FD results are taken from Graves (1996).

Fig. 15 shows a comparison between the two methods for $\eta = 0.25$ and $\eta = 0.50$. The agreement is excellent. In particular, the strong amplification close to the edges of the crater is reproduced well. Note that the amplification level of the vertical component reaches a very high value ($\simeq 3.2$) in the centre for $\eta = 0.50$. The horizontal component is zero in the centre by symmetry. Close to the edge, the horizontal component reaches 60 per cent of the amplitude of the incident wave for $\eta = 0.50$. The small discrepancy that can be observed between $x/a = 1$ and $x/a = 1.5$ km for $\eta = 0.50$ may be due to an underestimation in Sánchez-Sesma (1983) because subsequent studies of Mossessian & Dravinski (1989) and Luzón *et al.* (1997) also predict higher values in this region.

7.4 Homogeneous model with strong attenuation

In order to validate the way in which we have introduced attenuation in the SEM, we consider a 2-D homogeneous medium of size 2000 m × 2000 m. Strong attenuation represented by a constant $Q_P \simeq 30$ and a constant $Q_S \simeq 20$ is introduced. The relaxed (elastic) velocities of the medium are $c_p = 3000$ m s^{-1} for the P wave and $c_s = 2000$ m s^{-1} for the S wave. The density is 2000 kg m^{-3}. In light of the strong attenuation, we expect very significant physical velocity dispersion. Carcione *et al.* (1988) studied this problem with a Fourier method for a point force source, and also derived the analytical solution using the correspondence principle to compute the Green's function in the frequency domain. Their analytical results are used here for comparison. The source is a vertical force placed exactly in the middle of the model, at $x_s = z_s = 1000$ m. The time variation of the source is a Ricker wavelet with dominant frequency $f_0 = 18$ Hz and onset time $t_0 = 0.06$ s. The source we use has the same frequency content as that used by Carcione *et al.* (1988), that is, it has significant energy up to roughly 50 Hz. We do not use exactly the same source in order to avoid energy at zero frequency, and thus circumvent a potential problem in the computation of the analytical solution in the frequency domain (Carcione *et al.* 1988, Appendix B). The constant values $Q_P \simeq 30$ and $Q_S \simeq 20$ are mimicked using two standard linear solids; we use the optimal relaxation times computed by Carcione *et al.* (1988) for these two mechanisms.

The medium is discretized using 44×44 spectral elements, with a polynomial degree $N = 5$. Therefore, the global grid comprises $221 \times 221 = 48\,841$ points. As mentioned previously, we use an explicit second-order FD time scheme to march the weak form of the momentum equation, and a fourth-order Runge–Kutta scheme to march the strong form of the memory variable equations. Both schemes use the same time step

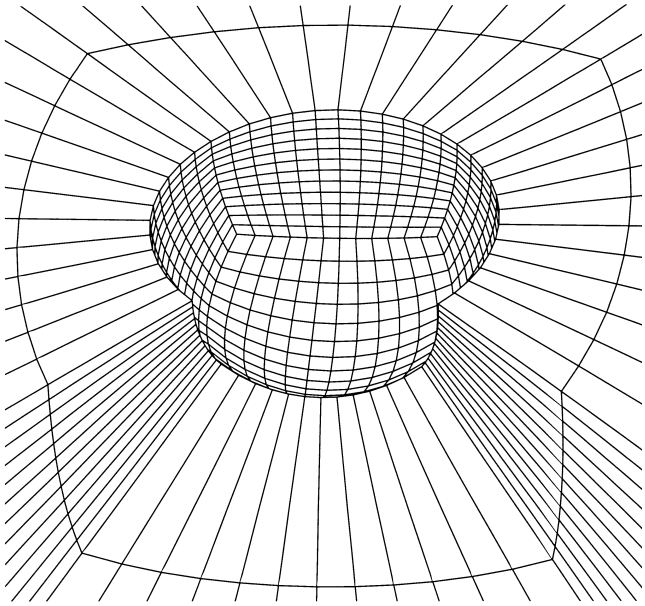

Figure 14. Close-up of the non-structured mesh based upon half a 'cubed sphere' used to define the grid for a hemispherical crater in a homogeneous half-space. The mesh is composed of five structured blocks. It is naturally adapted to the sharp edges of the crater and is densified in its vicinity. One can see the very big aspect ratio of the elements close to the crater, because in this simulation the main concern is the correct description of the geometry of the crater, not the number of points per wavelength, due to the low frequencies considered. For display purposes, one of the structured blocks has been removed.

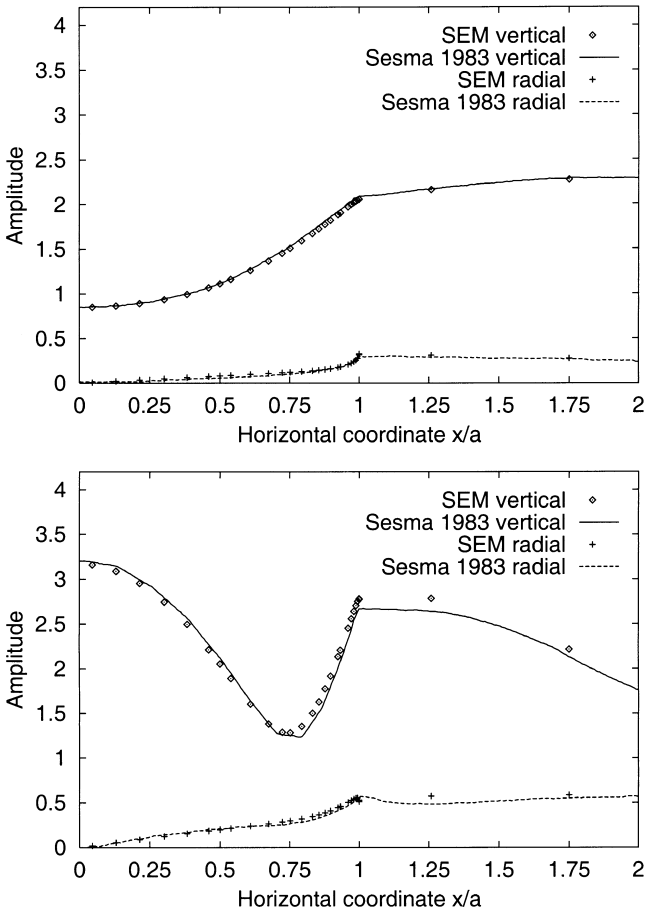

Figure 15. Amplitudes of the two components of displacement recorded along the crater, from $x/a=0$ (centre of the crater) to $x/a=2$ km. The vertical and radial components are displayed. The third (tangential) component is zero by symmetry. The results are shown for two normalized frequencies, $\eta=0.25$ (top) and $\eta=0.50$ (bottom). The symbols are used to show the SEM results. The solid and dashed lines are the results of Sánchez-Sesma (1983) obtained based upon an approximate boundary method.

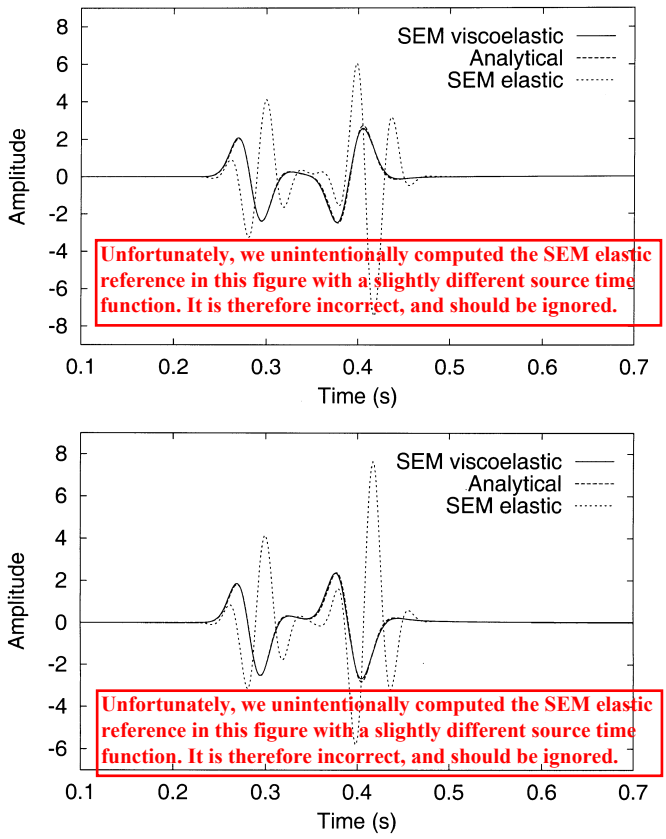

Figure 16. Amplitude of the horizontal (top) and vertical (bottom) components of displacement recorded in a 2-D homogeneous medium of size 2000 m $\times$ 2000 m with constant $Q_P \simeq 30$ and $Q_S \simeq 20$. The source is a vertical force placed exactly in the middle of the model. The constant Q values are mimicked using two standard linear solids. We present both the spectral element solution (solid line) and the analytical solution derived by Carcione *et al.* (1988) (dashed line) for a receiver located at $x_r = z_r = 1500$ m, that is, at a distance of 707.1 m from the source. The very strong effect of attenuation can be observed by comparing these results to the SEM solution computed for an elastic medium with the same relaxed material properties (dotted line).

$\Delta t = 0.75$ ms. We propagate the signal for 0.75 s, i.e. 1000 time steps. In Fig. 16 we present both the SEM solution and the analytical solution for a receiver located at $x_r = z_r = 1500$ m, that is, at a distance of 707.1 m from the source. The agreement is very good, which validates the approach used to incorporate attenuation. To show how strong the attenuation and associated velocity dispersion are, we also plot the SEM solution computed for an elastic medium with the same relaxed material properties (that is, the medium obtained when $Q \rightarrow \infty$). One can see, for instance, that the amplitude of the S wave is reduced by a factor of more than two.

8 CONCLUSIONS

We have presented a detailed introduction to the spectral element method for 3-D seismic wave propagation. The method incorporates surface topography, attenuation and anisotropy, and accurately represents surface waves. We have benchmarked the method against a discrete wavenumber/reflectivity method for layer-cake models. Even in the presence of very sharp discontinuities, for example, a factor of 3 increase in P-wave velocity, the method accurately models the propagation of both body and surface waves for shallow as well as deep sources. The technique accommodates point force and moment tensor sources, and can easily be extended to include finite sources. The accuracy of the free-surface implementation was demonstrated for the problem of a hemispherical crater embedded in a homogeneous half-space, for which an approximate boundary method was used as a reference. The effects of attenuation were incorporated based upon an absorption-band model. For a highly attenuating model with associated strong dispersion the accuracy of the method was demonstrated by comparison with an analytical solution.

In order to model wave propagation in realistic 3-D earth models, for instance to determine seismic risk associated with potential earthquakes in metropolitan areas such as Los Angeles, Tokyo or Mexico City, several difficult problems need to be addressed. First, we need to show that the SEM is capable of dealing with highly heterogeneous 3-D structures, including regions with high Poisson's ratio. This problem has been partially addressed in Komatitsch (1997) and Komatitsch & Vilotte (1998), but it remains to be shown that the method can

also deal with more realistic models. Second, detailed 3-D models of such basins, constructed based upon geological, well-log and seismic reflection and refraction data, need to be constructed, and for larger earthquakes the details of the rupture also have to be determined; several studies have been dedicated to these problems in recent years (e.g. Wald 1996; Olsen & Archuleta 1996; Pitarka *et al.* 1998; Wald & Graves 1998).

As underlined in the innovative work of Chaljub & Vilotte (1998), in the context of global seismology several obstacles need to be overcome. At long periods, self-gravitation is important and needs to be accommodated in the weak formulation of the equations of motion. To maintain a relatively constant number of gridpoints per wavelength, the mesh has to be coarsened several times as a function of depth. Finally, the core–mantle boundary is an extremely sharp fluid–solid interface that needs to be incorporated accurately. Even though the spectral element method has been successfully applied for problems involving a homogeneous fluid (Komatitsch *et al.* 1999a), it has to be extended to include inhomogeneous fluids.

ACKNOWLEDGMENTS

We are very grateful to Michel Bouchon for numerous discussions and for providing us with his 3-D DWN code. We would also like to thank Emmanuel Chaljub and Jean-Pierre Vilotte for fruitful discussion, in particular regarding the use of the cubed sphere, Robert W. Graves for providing us with his results for the moment tensor source, and Paul F. Fischer for providing us with his non-structured global numbering code. Discussions with Francisco-José Sánchez-Sesma regarding the solution of the hemispherical crater problem, and with José M. Carcione and Marwan Charara regarding the analytical solution of the attenuation problem are also acknowledged. We thank Robert W. Graves and an anonymous reviewer for constructive comments that improved the manuscript. The Caltech computer center CACR kindly gave us access to their PC cluster, and the DMPN at IPGP provided access to their DEC Alpha. This work was funded in part by the David and Lucile Packard Foundation, NSF and NEHRP.

REFERENCES

Bao, H., Bielak, J., Ghattas, O., Kallivokas, L.F., O'Hallaron, D.R., Shewchuk, J.R. & Xu, J., 1998. Large-scale simulation of elastic wave propagation in heterogeneous media on parallel computers, *Comp. Meth. appl. Mech. Eng.,* **152,** 85–102.

Bernardi, C., Debit, N. & Maday, Y., 1990. Coupling finite element and spectral methods: first results, *Math. Comput.,* **54,** 21–39.

Bouchon, M., 1981. A simple method to calculate Green's functions for elastic layered media, *Bull. seism. Soc. Am.,* **71,** 959–971.

Bouchon, M., Schultz, C.A. & Töksoz, M.N., 1996. Effect of three-dimensional topography on seismic motion, *J. geophys. Res.,* **101,** 5835–5846.

Canuto, C., Hussaini, M.Y., Quarteroni, A. & Zang, T.A., 1988. *Spectral Methods in Fluid Dynamics,* Springer-Verlag, New York.

Carcione, J.M., 1994. The wave equation in generalized coordinates, *Geophysics,* **59,** 1911–1919.

Carcione, J.M., Kosloff, D. & Kosloff, R., 1988. Wave propagation simulation in a linear viscoelastic medium, *Geophys. J. Int.,* **95,** 597–611.

Chaljub, E. & Vilotte, J.P., 1998. 3D wave propagation in a spherical earth model using the spectral element method, *EOS, Trans. Am. geophys. Un.,* **79,** F625–F626.

Clayton, R. & Engquist, B., 1977. Absorbing boundary conditions for acoustic and elastic wave equations, *Bull. seism. Soc. Am.,* **67,** 1529–1540.

Cohen, G., Joly, P. & Tordjman, N., 1993. Construction and analysis of higher-order finite elements with mass lumping for the wave equation, in *2nd Int. Conf. on Mathematical and Numerical Aspects of Wave Propagation,* ed. Kleinman, R., pp. 152–160, SIAM, Philadelphia.

Day, S.M., 1998. Efficient simulation of constant Q using coarse-grained memory variables, *Bull. seism. Soc. Am.,* **88,** 1051–1062.

Dhatt, G. & Touzot, G., 1984. *The Finite Element Method Displayed,* John Wiley, New York.

Emmerich, H. & Korn, M., 1987. Incorporation of attenuation into time-domain computations of seismic wave fields, *Geophysics,* **52,** 1252–1264.

Faccioli, E., Maggio, F., Paolucci, R. & Quarteroni, A., 1997. 2D and 3D elastic wave propagation by a pseudo-spectral domain decomposition method, *J. Seism.,* **1,** 237–251.

Fischer, P.F. & Rønquist, E.M., 1994. Spectral element methods for large scale parallel Navier-Stokes calculations, *Comp. Meth. appl. Mech. Eng.,* **116,** 69–76.

Furumura, T., Kennett, B.L.N. & Furumura, M., 1998. Seismic wavefield calculation for laterally heterogeneous whole earth models using the pseudospectral method, *Geophys. J. Int.,* **135,** 845–860.

Geller, R.J. & Ohminato, T., 1994. Computation of synthetic seismograms and their partial derivatives for heterogeneous media with arbitrary natural boundary conditions using the direct solution method, *Geophys. J. Int.,* **116,** 421–446.

Graves, R.W., 1996. Simulating seismic wave propagation in 3D elastic media using staggered-grid finite differences, *Bull. seism. Soc. Am.,* **86,** 1091–1106.

Guo, B. & Babuška, I., 1986. The *h-p* version of the finite element method, *Comp. Mech.,* **1,** 21–41.

Hughes, T.J.R., 1987. *The Finite Element Method, Linear Static and Dynamic Finite Element Analysis,* Prentice-Hall, Englewood Cliffs, NJ.

Igel, H., Mora, P. & Riollet, B., 1995. Anisotropic wave propagation through finite-difference grids, *Geophysics,* **60,** 1203–1216.

Kay, I. & Krebes, E.S., 1999. Applying finite element analysis to the memory variable formulation of wave propagation in anelastic media, *Geophysics,* **64,** 300–307.

Kelly, K.R., Ward, R.W., Treitel, S. & Alford, R.M., 1976. Synthetic seismograms: a finite difference approach, *Geophysics,* **41,** 2–27.

Komatitsch, D., 1997. Méthodes spectrales et éléments spectraux pour l'équation de l'élastodynamique 2D et 3D en milieu hétérogène, *PhD thesis,* Institut de Physique du Globe de Paris, Paris.

Komatitsch, D. & Vilotte, J.P., 1998. The spectral element method: an efficient tool to simulate the seismic response of 2D and 3D geological structures, *Bull. seism. Soc. Am.,* **88,** 368–392.

Komatitsch, D., Coutel, F. & Mora, P., 1996. Tensorial formulation of the wave equation for modelling curved interfaces, *Geophys. J. Int.,* **127,** 156–168.

Komatitsch, D., Barnes, C. & Tromp, J. 1999a. Wave propagation near a fluid-solid interface: a spectral element approach, *Geophysics,* in press.

Komatitsch, D., Barnes, C. & Tromp, J. 1999b. Simulation of anisotropic wave propagation based upon a spectral element method, *Geophysics,* submitted.

Komatitsch, D., Vilotte, J.P., Vai, R., Castillo-Covarrubias, J.M. & Sánchez-Sesma, F.J., 1999c. The spectral element method for elastic wave equations: application to 2D and 3D seismic problems, *Int. J. Num. Meth. Eng.,* **45,** 1139–1164.

Lahaye, D.J.P., Maggio, F. & Quarteroni, A., 1997. Hybrid finite element-spectral element approximation of wave propagation problems, *East-West J. Num. Math.,* **5,** 265–289.

Liu, H.P., Anderson, D.L. & Kanamori, H., 1976. Velocity dispersion due to anelasticity: implications for seismology and mantle composition, *Geophys. J. R. astr. Soc.,* **47,** 41–58.

Luzón, F., Sánchez-Sesma, F.J., Rodríguez-Zúñiga, J.L., Posadas, A.M., García, J.M., Martín, J., Romacho, M.D. & Navarro, M., 1997. Diffraction of *P*, *S* and Rayleigh waves by three-dimensional topographies, *Geophys. J. Int.,* **129,** 571–578.

Maday, Y. & Rønquist, E.M., 1990. Optimal error analysis of spectral methods with emphasis on non-constant coefficients and deformed geometries, *Comp. Meth. appl. Mech. Eng.,* **80,** 91–115.

Marfurt, K.J., 1984. Accuracy of finite-difference and finite-element modeling of the scalar wave equation, *Geophysics,* **49,** 533–549.

Moczo, P., Bystrický, E., Kristek, J., Carcione, J.M. & Bouchon, M., 1997. Hybrid modeling of *P-SV* seismic motion at inhomogeneous viscoelastic topographic structures, *Bull. seism. Soc. Am.,* **87,** 1305–1323.

Mossessian, T.K. & Dravinski, M., 1989. Scattering of elastic waves by three-dimensional surface topographies, *Wave Motion,* **11,** 579–592.

Müller, G., 1985. The reflectivity method: a tutorial, *J. Geophys.,* **58,** 153–174.

Ohminato, T. & Chouet, B.A., 1997. A free-surface boundary condition for including 3D topography in the finite difference method, *Bull. seism. Soc. Am.,* **87,** 494–515.

Olsen, K.B. & Archuleta, R.J., 1996. 3-D simulation of earthquakes on the Los Angeles fault system, *Bull. seism. Soc. Am.,* **86,** 575–596.

Paolucci, R., Faccioli, E. & Maggio, F., 1999. 3D response analysis of an instrumented hill at Matsuzaki, Japan, by a spectral method, *J. Seism.,* **3,** 191–209.

Patera, A.T., 1984. A spectral element method for fluid dynamics: laminar flow in a channel expansion, *J. Comput. Phys.,* **54,** 468–488.

Pitarka, A., Irikura, K., Iwata, T. & Sekiguchi, H., 1998. Three-dimensional simulation of the near-fault ground motion for the 1995 Hyogo-ken Nanbu (Kobe), Japan, earthquake, *Bull. seism. Soc. Am.,* **88,** 428–440.

Priolo, E., Carcione, J.M. & Seriani, G., 1994. Numerical simulation of interface waves by high-order spectral modeling techniques, *J. acoust. Soc. Am.,* **95,** 681–693.

Quarteroni, A., Tagliani, A. & Zampieri, E., 1998. Generalized Galerkin approximations of elastic waves with absorbing boundary conditions, *Comp. Meth. appl. Mech. Eng.,* **163,** 323–341.

Robertsson, J.O.A., 1996. A numerical free-surface condition for elastic/viscoelastic finite-difference modeling in the presence of topography, *Geophysics,* **61,** 1921–1934.

Robertsson, J.O.A., Blanch, J.O. & Symes, W.W., 1994. Viscoelastic finite-difference modeling, *Geophysics,* **59,** 1444–1456.

Ronchi, C., Ianoco, R. & Paolucci, P.S., 1996. The 'Cubed Sphere': a new method for the solution of partial differential equations in spherical geometry, *J. Comput. Phys.,* **124,** 93–114.

Sánchez-Sesma, F.J., 1983. Diffraction of elastic waves by three-dimensional surface irregularities, *Bull. seism. Soc. Am.,* **73,** 1621–1636.

Seriani, G., 1997. A parallel spectral element method for acoustic wave modeling, *J. Comput. Acoust.,* **5,** 53–69.

Seriani, G., 1998. 3-D large-scale wave propagation modeling by spectral element method on Cray T3E multiprocessor, *Comp. Meth. appl. Mech. Eng.,* **164,** 235–247.

Seriani, G. & Priolo, E., 1994. Spectral element method for acoustic wave simulation in heterogeneous media, *Finite Elements in Analysis and Design,* **16,** 337–348.

Seriani, G., Priolo, E., Carcione, J.M. & Padovani, E., 1992. High-order spectral element method for elastic wave modeling, in *Expanded abstracts of the SEG,* pp. 1285–1288, 62nd Int. Mtng of the SEG, New-Orleans.

Seriani, G., Priolo, E. & Pregarz, A., 1995. Modelling waves in anisotropic media by a spectral element method, in *Third Int. Conf. on Mathematical and Numerical Aspects of Wave Propagation,* ed. Cohen, G., pp. 289–298, SIAM, Philadelphia.

Tarnow, N. & Simo, J.C., 1994. How to render second-order accurate time-stepping algorithms fourth-order accurate while retaining the stability and conservation properties, *Comp. Meth. appl. Mech. Eng.,* **115,** 233–252.

Tessmer, E. & Kosloff, D., 1994. 3-D elastic modeling with surface topography by a Chebyshev spectral method, *Geophysics,* **59,** 464–473.

Tessmer, E., Kessler, D., Kosloff, D. & Behle, A., 1992. Multi-domain Chebyshev-Fourier method for the solution of the equations of motion of dynamic elasticity, *J. Comput. Phys.,* **100,** 355–363.

Virieux, J., 1986. *P-SV* wave propagation in heterogeneous media: velocity-stress finite-difference method, *Geophysics,* **51,** 889–901.

Wald, D.J., 1996. Slip history of the 1995 Kobe, Japan, earthquake determined from strong motion, teleseismic, and geodetic data, *J. Phys. Earth,* **44,** 489–503.

Wald, D.J. & Graves, R.W., 1998. The seismic responses of the Los Angeles basin, California, *Bull. seism. Soc. Am.,* **88,** 337–356.

Zeng, X., 1996. Finite difference modeling of viscoelastic wave propagation in a generally heterogeneous medium in the time domain, and a dissection method in the frequency domain, *PhD thesis,* University of Toronto, Canada.

Zienkiewicz, O.C., 1977. *The Finite Element Method in Engineering Science,* 3rd edn, McGraw-Hill, New York.

APPENDIX A: DETAILED DESCRIPTION OF THE WEAK FORMULATION

In this Appendix we present detailed expressions for each of the terms in the weak formulation of the equations of motion (12), suitable for numerical evaluation at the elemental level. The expression for the left-hand side of (12), the mass matrix, was discussed in Section 5. The remaining three terms on the right-hand side are presented here.

The first integral that needs to be evaluated at the elemental level is

$$\int_{\Omega_e} \nabla \mathbf{w} : \mathbf{T}\, d^3\mathbf{x}\,. \tag{A1}$$

This integral is often referred to as the elemental *stiffness matrix*. The first step is to calculate the nine elements of the displacement gradient $\nabla \mathbf{s}$ on the element Ω_e. This gives

$$\begin{aligned}\partial_i s_j(\mathbf{x}(\xi_\alpha, \eta_\beta, \zeta_\gamma), t) = &\left[\sum_{\sigma=0}^{n_\ell} s_j^{\sigma\beta\gamma}(t)\ell'_\sigma(\xi_\alpha)\right]\partial_i\xi(\xi_\alpha, \eta_\beta, \zeta_\gamma)\\ &+\left[\sum_{\sigma=0}^{n_\ell} s_j^{\alpha\sigma\gamma}(t)\ell'_\sigma(\eta_\beta)\right]\partial_i\eta(\xi_\alpha, \eta_\beta, \zeta_\gamma)\\ &+\left[\sum_{\sigma=0}^{n_\ell} s_j^{\alpha\beta\sigma}(t)\ell'_\sigma(\zeta_\gamma)\right]\partial_i\zeta(\xi_\alpha, \eta_\beta, \zeta_\gamma)\,.\end{aligned} \tag{A2}$$

This calculation requires knowledge of the nine elements of the inverse Jacobian matrix $\partial\boldsymbol{\xi}/\partial\mathbf{x}$. Next, one calculates the six elements of the symmetric stress tensor $\mathbf{T}$ on the element:

$$\mathbf{T}(\mathbf{x}(\xi_\alpha, \eta_\beta, \zeta_\gamma), t) = \mathbf{c}(\mathbf{x}(\xi_\alpha, \eta_\beta, \zeta_\gamma)) : \nabla\mathbf{s}(\mathbf{x}(\xi_\alpha, \eta_\beta, \zeta_\gamma), t)\,. \tag{A3}$$

This requires knowledge of the previously calculated displacement gradient (A2) and of the elastic tensor $\mathbf{c}$ at the Gauss–Lobatto–Legendre integration points. The formulation is not limited to isotropic media, or to anisotropic media with a high degree of symmetry, as is often the case for other numerical methods. The earth model may be fully heterogeneous, that is, $\mathbf{c}$ need not be constant inside an element. The

integrand $\nabla\mathbf{w}:\mathbf{T}$ may be written in the form

$$\nabla\mathbf{w}:\mathbf{T}=\sum_{i,j=1}^{3} T_{ij}\,\partial_j w_i=\sum_{i,k=1}^{3}\left(\sum_{j=1}^{3} T_{ij}\,\partial_j\xi_k\right)\frac{\partial w_i}{\partial\xi_k}$$
$$=\sum_{i,k=1}^{3} F_{ik}\,\frac{\partial w_i}{\partial\xi_k}\,, \tag{A4}$$

where

$$F_{ik}=\sum_{j=1}^{3} T_{ij}\,\partial_j\xi_k\,. \tag{A5}$$

The next step is to calculate the nine matrix elements F_{ik} on the Gauss–Lobatto–Legendre integration points: $F_{ik}^{\sigma\tau\nu}=F_{ik}(\mathbf{x}(\xi_\sigma,\eta_\tau,\zeta_\nu))$; this requires knowledge of the stress tensor $\mathbf{T}$ computed in (A3) and of the inverse Jacobian matrix $\partial\boldsymbol{\xi}/\partial\mathbf{x}$. The integral (A1) may now be rewritten in the form

$$\sum_{i,k=1}^{3}\int_{\Omega_e} F_{ik}\,\frac{\partial w_i}{\partial\xi_k}\,d^3\mathbf{x}=\sum_{i,k=1}^{3}\int_{-1}^{1}\int_{-1}^{1}\int_{-1}^{1} F_{ik}\,\frac{\partial w_i}{\partial\xi_k}\,J_e\,d\xi\,d\eta\,d\zeta\,. \tag{A6}$$

Upon substituting the test vector (35) in (A6) and introducing the Gauss–Lobatto–Legendre integration rule, we find that

$$\int_{\Omega_e}\nabla\mathbf{w}:\mathbf{T}\,d^3\mathbf{x}\approx\sum_{i=1}^{3} w_i^{\alpha\beta\gamma}\left[\omega_\beta\omega_\gamma\sum_{\alpha'=0}^{n_\ell}\omega_{\alpha'}J_e^{\alpha'\beta\gamma}F_{i1}^{\alpha'\beta\gamma}\ell'_\alpha(\xi_{\alpha'})\right.$$
$$+\omega_\alpha\omega_\gamma\sum_{\beta'=0}^{n_\ell}\omega_{\beta'}J_e^{\alpha\beta'\gamma}F_{i2}^{\alpha\beta'\gamma}\ell'_\beta(\eta_{\beta'})$$
$$\left.+\omega_\alpha\omega_\beta\sum_{\gamma'=0}^{n_\ell}\omega_{\gamma'}J_e^{\alpha\beta\gamma'}F_{i3}^{\alpha\beta\gamma'}\ell'_\gamma(\zeta_{\gamma'})\right]. \tag{A7}$$

The source term $\mathbf{M}:\nabla\mathbf{w}$ may be rewritten as

$$\mathbf{M}:\nabla\mathbf{w}=\sum_{i,j=1}^{3} M_{ij}\,\partial_j w_i=\sum_{i,k=1}^{3}\left(\sum_{j=1}^{3} M_{ij}\,\partial_j\xi_k\right)\frac{\partial w_i}{\partial\xi_k}$$
$$=\sum_{i,k=1}^{3} G_{ik}\,\frac{\partial w_i}{\partial\xi_k}\,, \tag{A8}$$

where

$$G_{ik}=\sum_{j=1}^{3} M_{ij}\,\partial_j\xi_k\,. \tag{A9}$$

Upon defining, as per usual, $G_{ik}^{\sigma\tau\nu}=G_{ik}(\mathbf{x}(\xi_\sigma,\eta_\tau,\zeta_\nu))$ and using the test vector (35),

$$\mathbf{M}:\nabla\mathbf{w}(\mathbf{x}_\mathrm{s})\approx\sum_{i=1}^{3} w_i^{\alpha\beta\gamma}\left\{\sum_{\sigma,\tau,\nu=0}^{n_\ell}\ell_\sigma(\xi_{\alpha_\mathrm{s}})\ell_\tau(\eta_{\beta_\mathrm{s}})\ell_\nu(\zeta_{\gamma_\mathrm{s}})\right.$$
$$\times[G_{i1}^{\sigma\tau\nu}\ell'_\alpha(\xi_{\alpha_\mathrm{s}})\ell_\beta(\eta_{\beta_\mathrm{s}})\ell_\gamma(\zeta_{\gamma_\mathrm{s}})$$
$$+G_{i2}^{\sigma\tau\nu}\ell_\alpha(\xi_{\alpha_\mathrm{s}})\ell'_\beta(\eta_{\beta_\mathrm{s}})\ell_\gamma(\zeta_{\beta_\mathrm{s}})$$
$$\left.+G_{i3}^{\sigma\tau\nu}\ell_\alpha(\xi_{\alpha_\mathrm{s}})\ell_\beta(\eta_{\beta_\mathrm{s}})\ell'_\gamma(\zeta_{\gamma_\mathrm{s}})]\right\}, \tag{A10}$$

where $\mathbf{x}(\xi_{\alpha_\mathrm{s}},\eta_{\beta_\mathrm{s}},\zeta_{\gamma_\mathrm{s}})=\mathbf{x}_\mathrm{s}$. If the source location $\mathbf{x}_\mathrm{s}$ coincides with one of the Gauss–Lobatto–Legendre points, (A10) reduces to

$$\mathbf{M}:\nabla\mathbf{w}(\mathbf{x}_\mathrm{s})\approx\sum_{i=1}^{3} w_i^{\alpha\beta\gamma}[G_{i1}^{\alpha_\mathrm{s}\beta_\mathrm{s}\gamma_\mathrm{s}}\ell'_\alpha(\xi_{\alpha_\mathrm{s}})\delta_{\beta\beta_\mathrm{s}}\delta_{\gamma\gamma_\mathrm{s}}$$
$$+G_{i2}^{\alpha_\mathrm{s}\beta_\mathrm{s}\gamma_\mathrm{s}}\delta_{\alpha\alpha_\mathrm{s}}\ell'_\beta(\eta_{\beta_\mathrm{s}})\delta_{\gamma\gamma_\mathrm{s}}+G_{i3}^{\alpha_\mathrm{s}\beta_\mathrm{s}\gamma_\mathrm{s}}\delta_{\alpha\alpha_\mathrm{s}}\delta_{\beta\beta_\mathrm{s}}\ell'_\gamma(\zeta_{\gamma_\mathrm{s}})]\,. \tag{A11}$$

In the case of a finite fault plane the mesh should be designed such that the fault coincides with the side of an element, that is, the fault is represented by a finite number of 'boundary elements'. In that case we have

$$\int_{S_\mathrm{s}}\mathbf{m}(\mathbf{x}_\mathrm{s},t):\nabla\mathbf{w}(\mathbf{x}_\mathrm{s})\,d^2\mathbf{x}_\mathrm{s}\approx\sum_{i=1}^{3} w_i^{\alpha\beta\gamma}\left[\omega_\beta\sum_{\alpha_\mathrm{s}=0}^{n_\ell}\omega_{\alpha_\mathrm{s}}J_b^{\alpha_\mathrm{s}\beta}g_{i1}^{\alpha_\mathrm{s}\beta\gamma}\ell'_\alpha(\xi_{\alpha_\mathrm{s}})\right.$$
$$+\omega_\alpha\sum_{\beta_\mathrm{s}=0}^{n_\ell}\omega_{\beta_\mathrm{s}}J_b^{\alpha\beta_\mathrm{s}}g_{i2}^{\alpha\beta_\mathrm{s}\gamma}\ell'_\beta(\eta_{\beta_\mathrm{s}})$$
$$\left.+\omega_\alpha\omega_\beta J_b^{\alpha\beta}g_{i3}^{\alpha\beta\gamma_\mathrm{s}}\ell'_\gamma(\zeta_{\gamma_\mathrm{s}})\right], \tag{A12}$$

where

$$g_{ik}=\sum_{j=1}^{3} m_{ij}\,\partial_j\xi_k \tag{A13}$$

and m_{ij} denotes the elements of the moment density tensor. Gridpoints within the fault plane are denoted by ξ_{α_s} and η_{β_s}, and gridpoints perpendicular to the fault plane are denoted by $\zeta_{\gamma_\mathrm{s}}$.

Finally, the absorbing boundary integral in (12) may be approximated at the elemental level as

$$\int_{\Gamma_e}\rho[v_n(\hat{\mathbf{n}}\cdot\partial_t\mathbf{s})\hat{\mathbf{n}}+v_1(\hat{\mathbf{t}}_1\cdot\partial_t\mathbf{s})\hat{\mathbf{t}}_1+v_2(\hat{\mathbf{t}}_2\cdot\partial_t\mathbf{s})\hat{\mathbf{t}}_2]\cdot\mathbf{w}\,d^2\mathbf{x}$$
$$\approx\sum_{i=1}^{3} w_i^{\alpha\beta\gamma}\left[\omega_\alpha\omega_\beta\,\rho^{\alpha\beta\gamma}\left(v_n^{\alpha\beta\gamma}\hat{n}_i\sum_{j=1}^{3}\hat{n}_j\dot{s}_j^{\alpha\beta\gamma}\right.\right.$$
$$\left.\left.+v_1^{\alpha\beta\gamma}\hat{t}_{1i}\sum_{j=1}^{3}\hat{t}_{1j}\dot{s}_j^{\alpha\beta\gamma}+v_2^{\alpha\beta\gamma}\hat{t}_{2i}\sum_{j=1}^{3}\hat{t}_{2j}\dot{s}_j^{\alpha\beta\gamma}\right)J_b^{\alpha\beta}\right]. \tag{A14}$$

Here ξ_α and η_β denote gridpoints within the absorbing boundary, and ζ_γ denotes gridpoints perpendicular to the boundary. Note that, like the mass matrix, the absorbing boundary term is diagonal.

In an anelastic medium, the stiffness matrix is still given by (A1), except that the stress tensor (A3) needs to be replaced by

$$\mathbf{T}(\mathbf{x}(\xi_\alpha,\eta_\beta,\zeta_\gamma),t)=\mathbf{c}(\mathbf{x}(\xi_\alpha,\eta_\beta,\zeta_\gamma)):\nabla\mathbf{s}(\mathbf{x}(\xi_\alpha,\eta_\beta,\zeta_\gamma),t)$$
$$-\sum_{\ell=1}^{L}\mathbf{R}^\ell(\mathbf{x}(\xi_\alpha,\eta_\beta,\zeta_\gamma),t)\,, \tag{A15}$$

in accordance with (5). The implication is that the six linearly independent components of the symmetric memory tensor $\mathbf{R}^\ell$ need to be stored on the grid. For this reason, the memory requirements for an anelastic simulation increase substantially over those for a purely elastic simulation, and it may in this respect be of interest to spread the memory variables across an element to obtain the expected behaviour (Day 1998).